The Astrophysical Journal, 678:1372–1395, 2008 May 10

ATMOSPHERIC PARAMETERS OF FIELD L AND T DWARFS[1]

Michael C. Cushing,[2] Mark S. Marley,[3] D. Saumon,[4] Brandon C. Kelly,[5] William D. Vacca,[6]
John T. Rayner,[7] Richard S. Freedman,[8] Katharina Lodders,[9] and Thomas L. Roellig[10]
Received 2007 June 27; accepted 2007 November 5

ABSTRACT

We present an analysis of the 0.95–14.5 μm spectral energy distributions of nine field ultracool dwarfs with spectral types ranging from L1 to T4.5. Effective temperatures, gravities, and condensate cloud sedimentation efficiencies are derived by comparing the data to synthetic spectra computed from atmospheric models that self-consistently include the formation of condensate clouds. Overall, the model spectra fit the data well, although the agreement at some wavelengths remains poor due to remaining inadequacies in the models. Derived effective temperatures decrease steadily through the L1–T4.5 spectral types, and we confirm that the effective temperatures of ultracool dwarfs at the L/T transition are nearly constant, decreasing by only ~200 K from spectral types L7.5 to T4.5. The condensate cloud properties vary significantly among the L dwarfs in our sample, ranging from very thick clouds to relatively thin clouds with no particular trend with spectral type. The two objects in our sample with very red $J - K_s$ colors are, however, best fitted with synthetic spectra that have thick clouds, which hints at a possible correlation between the near-infrared colors of L dwarfs and the condensate cloud properties. The fits to the two T dwarfs in our sample (T2 and T4.5) also suggest that the clouds become thinner in this spectral class, in agreement with previous studies. Restricting the fits to narrower wavelength ranges (i.e., individual photometric bands) almost always yields excellent agreement between the data and models. Limitations in our knowledge of the opacities of key absorbers such as FeH, VO, and CH_4 at certain wavelengths remain obvious, however. The effective temperatures obtained by fitting the narrower wavelength ranges can show a large scatter compared to the values derived by fitting the full spectral energy distributions; deviations are typically ~200 K and, in the worst cases, up to 700 K.

Subject headings: infrared: stars — radiative transfer — stars: fundamental parameters — stars: low-mass, brown dwarfs

1. INTRODUCTION

The emergent spectra of very low mass stars and brown dwarfs, collectively known as "ultracool dwarfs," are shaped in large part by gas and condensation chemistry. The low-temperature (500 K $\lesssim T \lesssim$ 3000 K), high-pressure (1 bar $\lesssim P \lesssim$ 10 bar) conditions typical of ultracool dwarf atmospheres favor the formation of molecules (such as CO, CH_4, N_2, NH_3, and H_2O) and, at $T < 2400$ K, condensates from the refractory elements (Ti, V, Ca, Al, Fe, Si, and Mg). Condensation removes gaseous opacity sources (such as TiO, VO, FeH, and CrH) from the atmosphere and alters the atmospheric chemistry as the condensates gravitationally settle and form clouds that deplete the upper layers of the atmosphere of both the condensates and their constituent elements (Fegley & Lodders 1994, 1996; Lodders 1999, 2002; Burrows & Sharp 1999). Condensates also contribute their own opacity, which can be substantial for the more abundant Fe-, Mg-, and Si-bearing species such as forsterite (Mg_2SiO_4), enstatite ($MgSiO_3$), and solid or liquid Fe (e.g., Marley et al. 2002; Tsuji 2002).

This rich chemistry gives rise to complex emergent spectra that are distinctly non-Planckian. The molecular line opacities dominate over all of the continuum opacity sources (e.g., H^-) that are important in the atmospheres of hotter stars (Allard & Hauschildt 1995), and as a result the emergent spectra of ultracool dwarfs exhibit strong molecular absorption bands of TiO, H_2O, and CH_4. Indeed, it is the strength of these and other molecular bands that are used to define the L and T spectral classes (Kirkpatrick et al. 1999; Burgasser et al. 2006b). L dwarf (2400 K $\lesssim T_{\rm eff} \lesssim$ 1400 K) spectra exhibit weakening TiO and VO bands at red optical wavelengths (0.6–1.0 μm) due to the formation of Ti-bearing condensates such as perovskite ($CaTiO_3$). The loss of the gaseous TiO and VO opacity results in a more transparent atmosphere and leads to the emergence of monatomic alkali lines (Na, K, Rb, and Cs). Most prominent are the resonance Na I ($\lambda\lambda$5890, 5896) and K I ($\lambda\lambda$7665, 7699) doublets, which become increasingly broad with later spectral type. At near-infrared wavelengths (1–2.5 μm) the L dwarfs also become progressively redder with later spectral types due to the additional condensate opacity. As CH_4 becomes the dominant carbon-bearing gas in the upper, coolest layers of the atmosphere (CO/CH_4 < 1 for $T \lesssim$ 1100 K at P = 1 bar), CH_4 absorption bands emerge at near-infrared wavelengths, which signals the transition between the L and T (1400 K $\lesssim T_{\rm eff} \lesssim$ 700 K) spectral classes. The K I and Na I resonance lines are present in the red optical spectra of T dwarfs (Burgasser et al. 2003a) because

[1] Based in part on data collected at the Subaru Telescope, which is operated by the National Astronomical Observatory of Japan.

[2] Steward Observatory, University of Arizona, 933 North Cherry Avenue, Tucson, AZ 85721. Current address: Institute of Astronomy, University of Hawaii, 2680 Woodlawn Drive, Honolulu, HI 96822; mcushing@ifa.hawaii.edu.
[3] NASA Ames Research Center, MS 254-3, Moffett Field, CA 94035; mark.s.marley@nasa.gov.
[4] Los Alamos National Laboratory, Applied Physics Division, MS F663, Los Alamos, NM 87545; dsaumon@lanl.gov.
[5] Steward Observatory, University of Arizona, 933 North Cherry Avenue, Tucson, AZ 85721; bkelly@as.arizona.edu.
[6] SOFIA-USRA, NASA Ames Research Center, MS N211-3, Moffett Field, CA 94035; wvacca@mail.arc.nasa.gov.
[7] Institute for Astronomy, University of Hawaii, 2680 Woodlawn Drive, Honolulu, HI 96822; rayner@ifa.hawaii.edu.
[8] SETI Institute, NASA Ames Research Center, MS 254-5, Moffett Field, CA 94035; freedman@darkstar.arc.nasa.gov.
[9] Planetary Chemistry Laboratory, Department of Earth and Planetary Sciences, Washington University, St. Louis, MO 63130; lodders@levee.wustl.edu.
[10] NASA Ames Research Center, MS N245-6, Moffett Field, CA 94035; thomas.l.roellig@nasa.gov.

TABLE 1
THE PROPERTIES OF THE L AND T DWARFS IN OUR SAMPLE

OBJECT	SPECTRAL TYPE[a]		J[b] (mag)	$J-H$ (mag)	$H-K_s$ (mag)	$J-K_s$ (mag)	π[c] (mas)	REFS.
	Optical	Infrared						
2MASS J14392836+1929149	L1	L1	12.759 ± 0.019	0.718 ± 0.027	0.495 ± 0.029	1.213 ± 0.029	69.6 ± 0.5	1, 5
2MASS J15065441+1321060	L3	...	13.365 ± 0.023	0.985 ± 0.031	0.639 ± 0.028	1.624 ± 0.030	...	6
2MASS J00361617+1821104	L3.5	L4 ± 1	12.466 ± 0.027	0.878 ± 0.040	0.530 ± 0.036	1.408 ± 0.034	114.2 ± 0.8	1, 7
2MASS J22244381−0158521	L4.5	L3.5	14.073 ± 0.027	1.255 ± 0.037	0.796 ± 0.035	2.051 ± 0.035	87.02 ± 0.89	1, 2, 8
2MASS J15074769−1627386	L5	L5.5	12.830 ± 0.027	0.935 ± 0.036	0.583 ± 0.035	1.518 ± 0.037	136.4 ± 0.6	1, 7
2MASS J08251968+2115521	L7.5	L6	15.100 ± 0.034	1.308 ± 0.047	0.764 ± 0.041	2.072 ± 0.043	94.22 ± 0.99	1, 2, 8
DENIS 025503.3−470049.0	L8	L9	13.246 ± 0.027	1.042 ± 0.036	0.646 ± 0.034	1.688 ± 0.036	201.37 ± 3.89	3, 9
SDSS J125453.90−012247.4	T2	T2	14.891 ± 0.035	0.801 ± 0.043	0.253 ± 0.060	1.054 ± 0.064	73.96 ± 1.59	2, 4, 10
2MASS J05591914−1404488	T5	T4.5	13.802 ± 0.024	0.123 ± 0.050	0.102 ± 0.068	0.225 ± 0.057	96.73 ± 0.96	1, 2, 11

[a] Spectral types of the L dwarfs are from Kirkpatrick et al. (1999, 2000), Reid et al. (2000), Gizis et al. (2000), Geballe et al. (2002), Knapp et al. (2004), Burgasser et al. (2006b), and J. D. Kirkpatrick (in preparation). Spectral types of the T dwarfs are from Burgasser et al. (2003a, 2006b). Errors on spectral types are ±0.5 subclass unless otherwise noted.

[b] J-, H-, and K_s-band photometry is from the 2MASS Point Source Catalog.

[c] Based on the weighted mean of the referenced parallaxes (Golimowski et al. 2004).

REFERENCES.—(1) Dahn et al. 2002; (2) Vrba et al. 2004; (3) Costa et al. 2006; (4) Tinney et al. 2003; (5) Kirkpatrick et al. 1999; (6) Gizis et al. 2000; (7) Reid et al. 2000; (8) Kirkpatrick et al. 2000; (9) Martín et al. 1999; (10) Leggett et al. 2000; (11) Burgasser et al. 2000.

the high-temperature condensate anorthite ($CaAl_2Si_2O_8$), a feldspar, has gravitationally settled out of the cooler atmospheric regions. In the absence of such settling, Na and K would condense into a feldspar in the form of albite ($NaAlSi_3O_8$) and orthoclase ($KAlSi_3O_8$) (Burrows & Sharp 1999; Lodders 1999; Marley et al. 2002).

The observed spectra and photometry of ultracool dwarfs can therefore serve as touchstones against which we can test our understanding of atmospheric physics, chemistry, dynamics, and cloud processes as embodied in our atmospheric models. Shortly after the discovery of the first bona fide brown dwarf, Gliese 229B (Nakajima et al. 1995), a number of publications appeared comparing the observed spectrum to models (Allard et al. 1996; Marley et al. 1996; Tsuji et al. 1996). Burrows et al. (2001) presented a review of the substantial subsequent work devoted to understanding the properties of L and T dwarfs. Although the comparison of models to the spectra of individual objects such as Gl 229B (Saumon et al. 2000) and Gl 570D (Geballe et al. 2001; Saumon et al. 2006) has played an important role in the progression of the field, relatively little work has been done on comparing entire classes of models to uniform data sets (see, however, Burgasser et al. 2006a). Such comparisons are important, as they can reveal the global properties of a set of objects and highlight the systematic strengths and weaknesses of the models.

In this work, we present such a comparison to one particular set of atmospheric models (Marley et al. 2002; M. S. Marley et al. 2008, in preparation). We aim to understand what the modeling has accomplished to date and to help direct future models and observations along the pathways that seem most promising. The paper is organized as follows. Sections 2 and 3 present the data and model atmospheres, respectively, used in the analysis. In § 4 we present the results of the comparisons between the data and models, and in § 5 we discuss two systematic uncertainties that affect our analysis.

2. THE DATA

There are currently 11 L and T dwarfs that have published spectra with nearly complete wavelength coverage from 0.65 to 14.5 μm (Cushing et al. 2006; Saumon et al. 2007). We selected the five L and two T dwarfs from the Cushing et al. sample with the highest signal-to-noise ratio (S/N) spectra that are not known to be multiple systems. We also included two additional L dwarfs, 2MASS J1506514+1321060 and DENIS J025503.3−470049.0, that were not part of the Cushing et al. sample. The properties of the dwarfs in our sample, including optical and infrared spectral types and Two Micron All Sky Survey (2MASS; Skrutskie et al. 2006) photometry, are given in Table 1. Although both optical and infrared spectral types are listed in Table 1, we hereafter use optical types for the L dwarfs (Kirkpatrick et al. 1999) and infrared types for the T dwarfs (Burgasser et al. 2006b). In addition, we abbreviate the numerical portions of the 2MASS, Sloan Digital Sky Survey (SDSS; York et al. 2000), and Deep Near Infrared Survey of the Southern Sky (DENIS; Epchtein et al. 1997) target designations as hhmm±ddmm, where the suffix is the sexigesimal right ascension (hours and minutes) and declination (degrees and arcminutes) at J2000.0 equinox.

The 0.65–14.5 μm spectra used in this work were constructed from the following sources: red optical spectra were obtained with the Low Resolution Imaging Spectrograph (LRIS; Oke et al. 1995) at the Keck telescope; near-infrared spectra were obtained with SpeX (Rayner et al. 2003) at the NASA IRTF and with the Infrared Camera and Spectrograph (IRCS; Kobayashi et al. 2000) on Subaru; and mid-infrared (5.5–14.5 μm) spectra were obtained with the Infrared Spectrograph (IRS; Houck et al. 2004) on board the *Spitzer Space Telescope* (Werner et al. 2004). The only wavelengths not covered by these spectra are those containing the strong telluric absorption bands at 1.9 and 2.6 μm and the 4.5–5.5 μm range. The latter wavelength range is exceedingly difficult to observe from the ground and is not covered by the IRS. Table 2 lists both the references and resolving powers ($R \equiv \lambda/\Delta\lambda$) of the various spectra used in this work. For each dwarf, the different spectra were absolutely flux-calibrated using ground-based photometry and then combined into a single 0.65–14.5 μm spectrum as described in Cushing et al. (2005, 2006).

Figure 1 shows the 2MASS $J-H$, $H-K_s$, and $J-K_s$ colors as a function of spectral type for all of the L and T dwarfs listed on the DwarfArchives[11] Web site as of 2007 June 7. The dwarfs in our sample are shown as red points. Overall, our sample is representative of dwarfs with similar spectral types. However, 2MASS 2224−0158 (L4.5) and 2MASS 0825+2115 (L7.5) have relatively

[11] See http://DwarfArchives.org.

TABLE 2
Spectral Characteristics of Ultracool Dwarfs in Our Sample

Object (1)	$R = \lambda/\Delta\lambda$ 0.6–0.9 μm (2)	0.9–2.5 μm (3)	3.0–4.1 μm (4)	5.5–14.5 μm (5)	References[a] (6)
2MASS J1439+1929	890	2000	940	90	1, 2, 2, 3
2MASS J1506+1321	890	2000	940	90	4, 2, 2, 3
2MASS J0036+1821	890	2000	940	90	5, 2, 2, 3
2MASS J2224−0158	890	2000	425	90	6, 2, 2, 3
2MASS J1507−1627	890	2000	940	90	5, 2, 2, 3
2MASS J0825+2115	890	1200	210	90	6, 2, 2, 3
DENIS 0255−4700	890	2000	210	90	7, 2, 2, 3
SDSS J1254−0122	1200	1200	210	90	8, 2, 2, 3
2MASS J0559−1404	1200	1200	210	90	8, 2, 2, 3

[a] The numbers in col. (6) indicate the references for each of the wavelength ranges given in cols. (2)–(5).

References.—(1) Kirkpatrick et al. 1999; (2) Cushing et al. 2005; (3) Cushing et al. 2006; (4) Gizis et al. 2000; (5) Reid et al. 2000; (6) Kirkpatrick et al. 2000; (7) J. D. Kirkpatrick 2007, private communication; (8) Burgasser et al. 2003a.

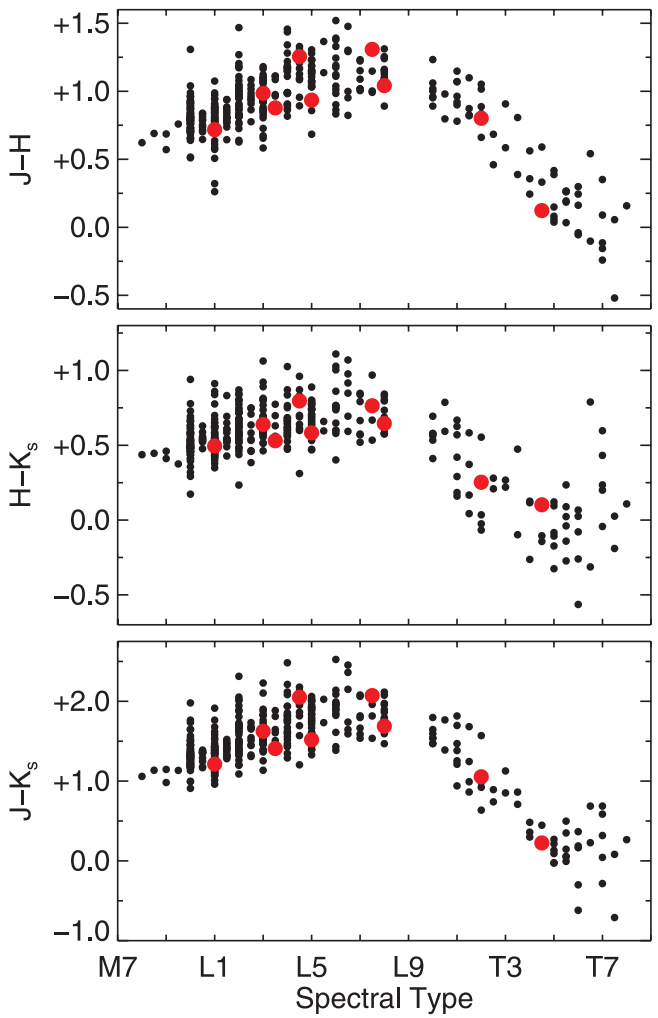

Fig. 1.—2MASS $J - H$ (*top*), $H - K_s$ (*middle*), and $J - K_s$ (*bottom*) colors as a function of spectral type for all of the L and T dwarfs in the DwarfArchives Web site as of 2007 June 7. The dwarfs in our sample are shown in red.

red $J - K_s$ colors given their spectral types, and 2MASS J1507−1627 (L5) has a relatively blue $J - K_s$ color. We discuss these dwarfs in more detail in § 4.6.

3. THE MODELS

The L and T dwarf models presented here have been produced in the same way as those in our earlier work (e.g., Marley et al. 1996, 2002; Burrows et al. 1997; Saumon et al. 2006). We are preparing a complete description of the models for a future publication. Briefly, we computed a grid of one-dimensional, plane-parallel, hydrostatic, nongray, radiative-convective equilibrium atmosphere models using our standard modeling code. A one-dimensional, plane-parallel approximation is appropriate, since the atmospheric scale height is always much smaller than the ultracool dwarf radius. We do not use mixing-length theory, but rather set the local lapse rate in the convective regions to the adiabatic lapse rate. This is an excellent approximation in the dense, warm atmospheres of brown dwarfs and giant planets where convection is a very efficient energy transport mechanism. The superadiabaticity is very small, and the atmospheric profile is insensitive to the choice of mixing length (Baraffe et al. 1997; Allard et al. 1997).

For the chemical equilibrium calculations we use the elemental abundance data of Lodders (2003) and compute compositions following Fegley & Lodders (1994), Lodders & Fegley (2002), and Lodders (1999, 2002). The chemical equilibrium abundances are computed for local thermodynamic equilibrium conditions. In stellar atmospheres, departures from thermochemical equilibrium can arise from interactions of atoms and molecules with the nonthermal radiation field, while in planetary atmospheres, nonequilibrium conditions can arise from vertical transport (by convection or eddy diffusion) on a timescale shorter than that of the chemical reactions involved. In ultracool dwarf atmospheres, the first effect is negligible compared to the second. In the present work, we neglect both effects. The opacity database includes the molecular lines of H_2O, CH_4, CO, NH_3, H_2S, PH_3, TiO, VO, CrH, FeH, CO_2, HCN, C_2H_2, C_2H_4, and C_2H_6; the atomic lines of the alkali metals (Li, Na, K, Rb, and Cs); continuum opacity from H_2 collision-induced absorption (CIA); Rayleigh scattering from H_2, H, and He; bound-free opacity from H, H^-, and H_2^+; and free-free opacity from He, H_2^-, and H_2^+. The molecular line lists are continually updated, and while they have well-known shortcomings, they represent the state of the art. An explanation of the treatment of line broadening and further details regarding the chemical equilibrium

calculation are presented in Freedman et al. (2008). Note that we do not include a turbulent velocity in the calculation of line shapes, as test calculations have shown this has a negligible effect for the temperatures and pressures considered here. An error in the TiO line opacity database (Schwenke 1998) employed in our recent generations of models (including those in Marley et al. [2002], Burgasser et al. [2002a], and Knapp et al. [2004]) that resulted in too-strong TiO absorption has been corrected.

For the model atmosphere calculation we use the *k*-coefficient method to describe the opacities (Goody et al. 1989). Within each of 180 spectral bins we sum the opacity arising from *each* of the several hundred million atomic and molecular lines in our database. Our radiative transfer follows the source function technique (Toon et al. 1989), allowing inclusion of arbitrary Mie scattering particles in the layer opacities. This approach is exact in the limit of single scattering and treats multiple scattering by assuming that the scattered radiation field can be approximated with two streams. After computing a pressure-temperature (P/T) profile with the *k*-coefficient method for a given set of parameters, we compute a high-resolution spectrum by solving the monochromatic radiative transfer equation for a larger number of frequency points (typically, ~190,000 in the range of 0.4–50 μm), using the exact same molecular line lists, continuum opacity sources, chemical composition, and line profiles as used for the computation of the *k*-coefficients. The resulting spectra can be smoothed or binned for comparison with data. Previous applications of our atmospheres code include the generation of P/T profiles and spectra for Titan (McKay et al. 1989), Uranus (Marley & McKay 1999), hot Jupiters (Fortney et al. 2005, 2006), and brown dwarfs (Marley et al. 1996, 2002; Burrows et al. 1997; Saumon et al. 2006).

As we converge to a model P/T profile, we compute the condensate size and vertical profiles following the prescription of Ackerman & Marley (2001) for various values of the cloud sedimentation efficiency parameter, $f_{\rm sed}$. Larger values of $f_{\rm sed}$ imply larger particle sizes and thus greater sedimentation efficiency. The width of the lognormal particle size distribution is set at $\sigma = 2$, and the eddy diffusion coefficient above the convective region is set to $K_{zz} = 10^5$ cm^2 s^{-1}. This latter value is consistent with that found from studies of the effect of nonequilibrium chemistry in L and T dwarf atmospheres (Saumon et al. 2006; Leggett et al. 2007). For any P/T profile there is a single description of the variation in particle sizes and number densities with altitude for each of the condensed species. As the atmospheric structure is iterated toward the equilibrium solution the cloud description is also continuously updated. The final result is a single, self-consistent thermal and cloud profile with the specified gravity, effective temperature, and cloud sedimentation efficiency. We term these models "cloudy." We also consider models in which the condensate formation is included in the chemical equilibrium calculation but the condensate opacity is neglected. We call these models "clear" and denote them as $f_{\rm sed} = $ nc, since the models include "no cloud" opacity.

In this first study, for the sake of simplicity, we consider a model parameter space consisting of $T_{\rm eff}$, g, and $f_{\rm sed}$ at solar metallicity. A more extensive study including variations in metallicity and other cloud parameters, as well as departures from chemical equilibrium caused by vertical mixing in the atmosphere (e.g., Saumon et al. 2006), will be the subject of future papers. Evolutionary models predict that field L and T dwarfs with ages greater than a few hundred million years have 700 K $\lesssim T_{\rm eff} \lesssim$ 2400 K and 5.0 $\lesssim \log g$(cm s^{-2}) $\lesssim$ 5.5 (Burrows et al. 1997). We consider the entire range of $T_{\rm eff}$ in steps of 100 K and values of $\log g$ of 4.5, 5.0, and 5.5. In previous work we found that $f_{\rm sed} \sim 3$ best reproduces the global properties of Jupiter's ammonia cloud (Ackerman & Marley 2001) and the $J - K$ colors of L dwarfs (e.g., Knapp et al. 2004). However, the excess TiO opacity in our previous models, particularly in the J band, may have led us to overestimate the $f_{\rm sed}$ value for L dwarfs. Accordingly, here we consider models with $f_{\rm sed} = 1$, 2, 3, 4, and nc. The final grid contains 270 models.

Dynamical processes in the atmospheres of individual objects ultimately control the growth and sedimentation of condensates and the optical properties of the various cloud decks expected in these atmospheres (e.g., Helling et al. 2001, 2004; Woitke & Helling 2003, 2004; Helling & Woitke 2006). Although our modeling parameter, $f_{\rm sed}$, aims to self-consistently capture these processes in a tractable way, the global properties of each individual object must ultimately define the true properties of the clouds. However, we do not yet understand how differences in metallicity, rotation rate, effective temperature, and gravity might manifest themselves as different values of $f_{\rm sed}$. Therefore, while we treat this parameter on the same footing as g and $T_{\rm eff}$ for fitting purposes, we recognize that, ultimately, more complete models would find that $f_{\rm sed}$ is determined by the global physical properties of individual objects.

For each combination of gravity, effective temperature, and sedimentation efficiency, we compute a self-consistent atmospheric P/T profile. Using this profile and employing the same atmospheric chemistry and opacities, we compute a high-resolution synthetic spectrum. This spectrum is then smoothed to the resolving power of the data using a Gaussian kernel and resampled onto the same wavelength grid. Figures 2 and 3 show a sequence of synthetic spectra, smoothed to $R = 500$ for clarity, with atmospheric parameters typical of an L dwarf ($T_{\rm eff} = 1800$ K, $\log g = 5.0$, $f_{\rm sed} = 2$) and a T dwarf ($T_{\rm eff} = 1100$ K, $\log g = 5.0$, $f_{\rm sed} =$ nc). The three panels in each figure illustrate the variations in spectral morphology when just one of the three parameters is changed.

The top panels show the changes in spectral morphology due to variations in $T_{\rm eff}$ at a fixed g and $f_{\rm sed}$. With decreasing $T_{\rm eff}$, the L dwarfs (Fig. 2) become redder in the near-infrared and the depths of the H_2O bands become deeper. Note also that the Q-branch of the ν_3 fundamental band of CH_4 at 3.3 μm is present at $T_{\rm eff} =$ 1700 K. The depths of the H_2O, CH_4, and NH_3 bands in the spectra of the T dwarfs (Fig. 3) become deeper with decreasing $T_{\rm eff}$, but in contrast to the L dwarfs, the T dwarfs become slightly bluer in the near-infrared.

The middle panels show the changes in spectral morphology due to variations in g at a fixed $T_{\rm eff}$ and $f_{\rm sed}$. In the L dwarfs the primary effect of increasing g is to weaken the near-infrared H_2O absorption bands. At these temperatures, the molecular abundances of H_2O and CH_4 depend weakly on the atmospheric pressure and are thus not sensitive to changes in gravity. The change in the H_2O band strengths is instead a result of the fact that, at a given pressure level in the atmosphere, the higher gravity models are cooler and as a result have thicker condensate clouds. The clouds produce a grayer emergent spectrum and are therefore responsible for the decreased depth of the H_2O bands. In contrast to the L dwarfs, the H_2O and CH_4 band depths in the spectra of T dwarfs are only marginally affected by changes in g, except in the K band. The peak flux level in the K band diminishes with increasing g due to an increase in the CIA of H_2. This broad, featureless absorption band (e.g., Borysow et al. 1997) centered at 2.4 μm is very sensitive to atmospheric pressure, and thus g, since it involves the collisions of particles ($\kappa_\nu \propto n_{\rm gas}^2$, where $n_{\rm gas}$ is the number density of the gas).

Finally, the bottom panels show the changes in spectral morphology due to variations in the cloud sedimentation parameter

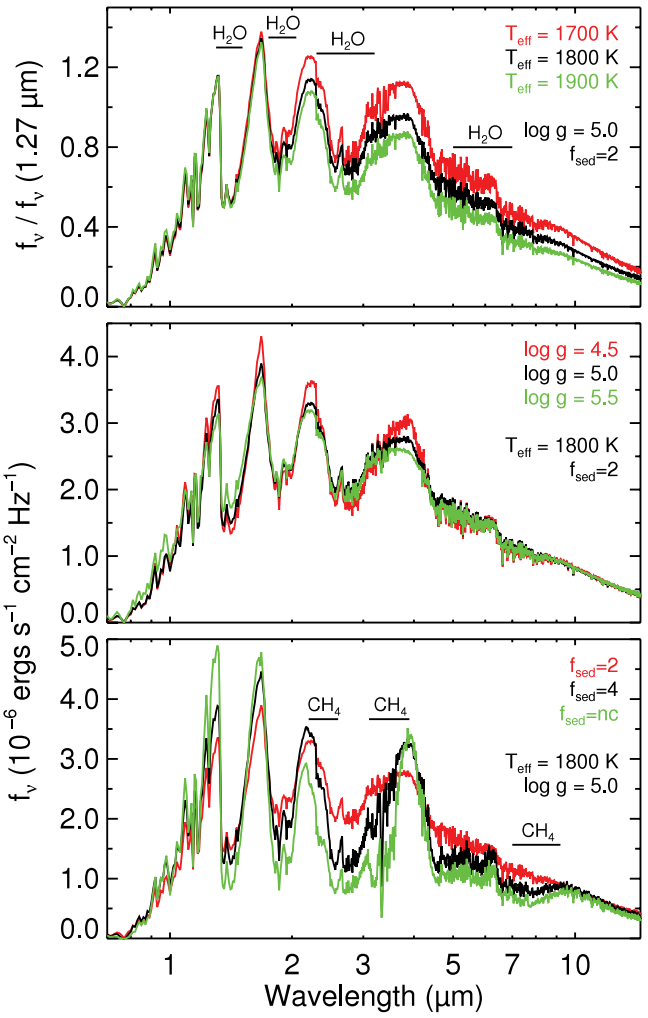

FIG. 2.—Comparison of synthetic spectra with atmospheric parameters typical of an L dwarf ($T_{\rm eff}$ = 1800 K, log g = 5.0, $f_{\rm sed}$ = 2) when $T_{\rm eff}$, log g, and $f_{\rm sed}$ are varied. The models have been smoothed to R = 500 and normalized to unity at 1.27 μm in the top panel to show the relative variations in the models as a function of $T_{\rm eff}$. The flux density units of the models in the middle and bottom panels correspond to the emergent flux at the top of the atmosphere.

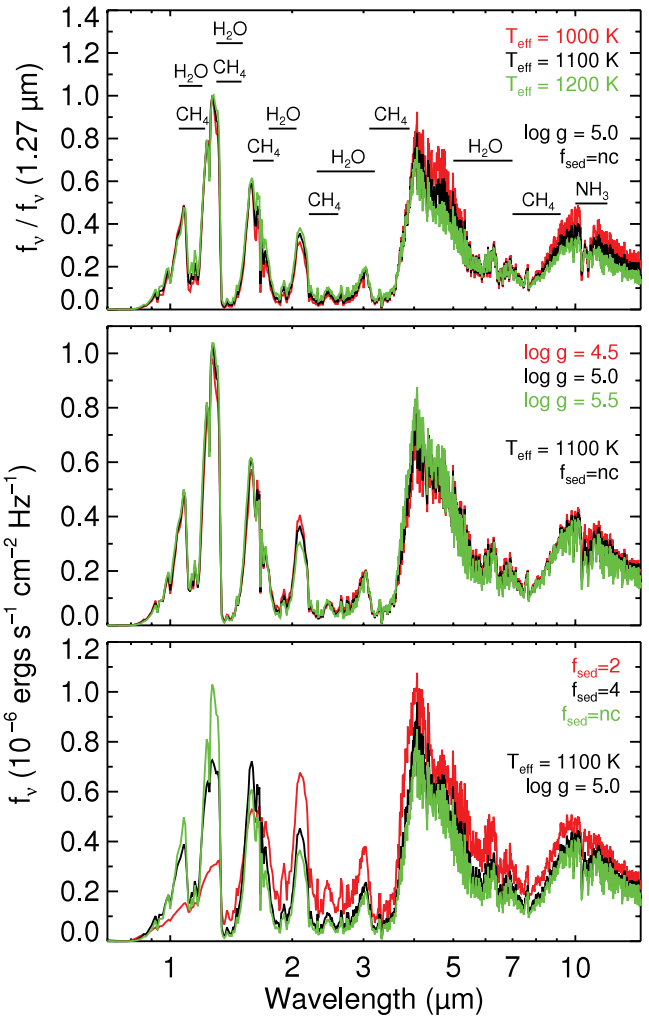

FIG. 3.—Same as Fig. 2, but for the atmospheric parameters of a typical T dwarf ($T_{\rm eff}$ = 1100 K, log g = 5.0, $f_{\rm sed}$ = nc).

$f_{\rm sed}$ at a fixed $T_{\rm eff}$ and g. Changes in $f_{\rm sed}$ produce the most dramatic variations in spectral morphology (particularly in the 1–6 μm region) underscoring the importance of correctly modeling the formation and subsequent sedimentation of condensates. The additional condensate opacity results in emergent spectra that are redder at near-infrared wavelengths than those from the cloudless models ($f_{\rm sed}$ = nc). The impact of the clouds on the emergent spectra of ultracool dwarfs becomes more dramatic with lower $f_{\rm sed}$ values because the clouds are thicker and thus contribute more opacity to the atmosphere.

4. ATMOSPHERIC PARAMETERS OF L AND T DWARFS

4.1. *Fitting Technique*

The one-dimensional model atmospheres predict the emergent flux density $\mathcal{F}_\nu$ ($\mathcal{F}_\nu = 2\pi \int_0^\infty I_\nu \mu\, d\mu$) as a function of wavelength (i.e., a synthetic spectrum) at the surface of a star. The synthetic spectra must be multiplied by $(R/d)^2$, where R is the stellar radius and d is the stellar distance, in order to obtain fluxes at Earth and directly compare them to observations. Although the parallaxes of nearly 80 L and T dwarfs have been measured (e.g., Dahn et al. 2002; Tinney et al. 2003; Vrba et al. 2004; Costa et al. 2006), the radii of field L and T dwarfs are currently unknown. Therefore, we can compare only the relative shapes of the modeled spectral energy distributions (SEDs) to the data.

For each model k, hereafter denoted by the triplet [$T_{\rm eff}$/log g/$f_{\rm sed}$], we compute a goodness-of-fit statistic G_k defined by[12]

$$G_k = \sum_{i=1}^{n} w_i \left(\frac{f_i - C_k \mathcal{F}_{k,i}}{\sigma_i} \right)^2, \qquad (1)$$

where n is the number of data pixels; w_i is the weight for the ith wavelength; f_i and $\mathcal{F}_{k,i}$ are the flux densities of the data and model k, respectively; σ_i are the errors in the observed flux densities; and C_k is the unknown multiplicative constant equal to $(R/d)^2$. For each model k, the constant C_k is determined by minimizing G_k with respect to C_k and is given by

$$C_k = \frac{\sum w_i f_i \mathcal{F}_{k,i}/\sigma_i^2}{\sum w_i \mathcal{F}_{k,i}^2/\sigma_i^2}. \qquad (2)$$

[12] We also tested the usefulness of the statistic $G_k = \sum_{i=1}^{n} w_i [(f_i - C\mathcal{F}_{k,i})/f_i]^2$, since most published spectra do not have errors associated with the flux density values. However, as noted by Takeda (1995), such a statistic gives more weight to wavelengths with low flux values. Typically, ultracool dwarf spectra have very low S/Ns at such wavelengths; thus, care must be taken when using such a statistic.

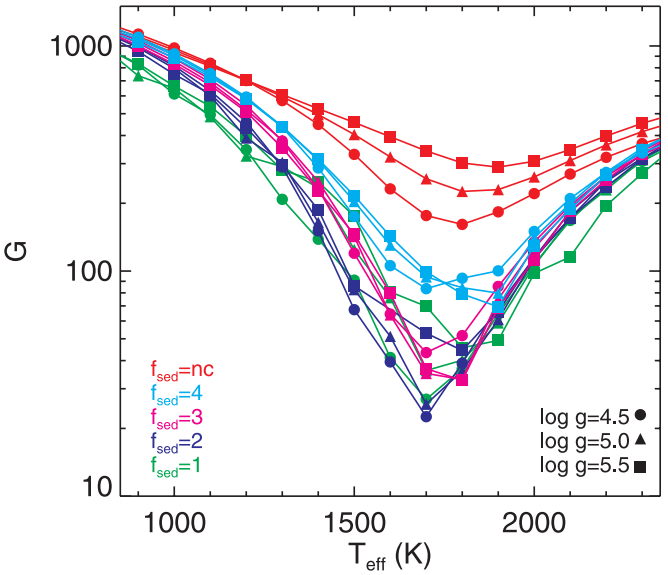

FIG. 4.—G values as a function of $T_{\rm eff}$ for the 0.95–14.5 μm spectrum of 2MASS 1507−1627 (L5). There is a clear minimum in G at 1700 K.

We select the best-fitting synthetic spectrum by locating the global minimum of the G values for all of the model spectra in our grid.

We have no a priori reason to favor one wavelength range over another; therefore, in principle, all wavelength points could receive equal weight in our fits. However, given the large variation in the wavelength sampling of our data (e.g., the near-infrared spectra cover only $\sim$2 μm but have $\sim$20 times more wavelength points than the *Spitzer* IRS spectra, which cover $\sim$10 μm), G would be heavily biased toward near-infrared wavelengths if w_i was set to unity for all i. We therefore choose to weight each pixel by its width in microns ($w_i = \Delta\lambda_i$). In § 5.2 we discuss the systematic effects that our choice of weights has on our results. Since the line lists of CH_4 are incomplete in the H band (Burrows et al. 2001; Freedman et al. 2008), and the $E^4\Pi - A^4\Pi$ system of FeH at 1.6 μm, which is present in the spectra of the L dwarfs (Wallace & Hinkle 2001; Cushing et al. 2003), lacks a line list, we also set the weights of the pixels from 1.58 to 1.75 μm (roughly the center of the H band) to zero.

As an example of our procedure, Figure 4 shows the G values of all the synthetic spectra in our grid as a function of $T_{\rm eff}$ computed for the spectrum of 2MASS 1507−1627 (L5). In this case, the best-fitting synthetic spectrum has the parameters [1700/4.5/2]. However, there are additional synthetic spectra that yield similar minimum G values. How, then, can we determine the quality of a given fit? Although G is mathematically similar to the χ^2 statistic, it does not follow a χ^2 distribution,[13] and as a result we cannot employ standard hypothesis testing techniques to assess the quality of the fits.

We therefore perform a Monte Carlo simulation to determine the range of synthetic spectra that fit the data given the observational errors. For each observed spectrum, we generate 2000 simulated data sets, wherein the flux at each wavelength point is randomly drawn from a Gaussian distribution centered on the observed flux, and with a width given by the observed variance in the individual pixel. Since each 0.65–14.5 μm spectrum is constructed by combining spectra that were absolutely flux-calibrated independently, the error in any given flux density value also includes a correlated component that arises from the fact that during the absolute flux-calibration process, all of the flux density values over a range of wavelengths (e.g., 1–2.5 μm) are scaled by a constant to adjust the overall flux level to match broadband photometry. We therefore scale the simulated flux density values by $10^{-0.4K}$, where K is randomly drawn from a Gaussian distribution centered on zero, and with a width given by the variance of the photometry (in magnitudes).

A simulated data set s_i is constructed from m spectra, each having its own $\sigma^2_{\rm ph}$. For a given spectrum j, the simulated data set s_i is given by

$$s_i = \mathcal{N}\left(f_i, \sigma_i^2\right) 10^{-0.4\mathcal{N}\left(0,\sigma^2_{{\rm ph},j}\right)}, \quad (3)$$

where $\mathcal{N}(\mu, \sigma^2)$ represents a value randomly drawn from a Gaussian distribution with mean μ and variance σ^2 and $\sigma^2_{{\rm ph},j}$ is the variance of the photometry used to absolutely flux-calibrate the spectrum j. We then replace f_i with s_i in equations (1) and (2) and recompute the best-fitting synthetic spectrum. The quality of the fit between the data and a given synthetic spectrum is given by $f_{\rm MC}$, the fraction of the 2000 simulations in which the given synthetic spectrum is identified as the best-fitting spectrum. In the case described above, the synthetic spectrum with the parameters [1700/4.5/2] has $f_{\rm MC} = 1.000$ and thus is the best representation of the data in our grid of synthetic spectra. Values of $f_{\rm MC}$ much less than unity imply that more than one synthetic spectrum in the grid fits the data well.

The best-fitting model parameters are given on the model grid points without interpolation. Nominally, this would give an internal uncertainty of half of the grid spacing, or $\pm$50 K in $T_{\rm eff}$, $\pm$0.25 in log g, and $\pm$0.5 in $f_{\rm sed}$. In practice, the best-fitting models nearly all have $f_{\rm MC} \sim 1$, which shows that the internal uncertainties on the fitting parameters are even smaller than those nominal values. As we see in § 5, our fits of the ultracool dwarf SEDs are affected by systematic effects that dominate the internal uncertainties and that are difficult to quantify. In addition, changes in the models (e.g., the inclusion of [Fe/H] as an additional parameter) or the use of a different goodness-of-fit statistic could yield different atmospheric parameters than we find here. An accurate determination of physical parameters of ultracool dwarfs will therefore require the development of more complete model atmospheres. Nonetheless, trends in the fitted parameters as revealed by this work should improve our understanding of the physics of ultracool dwarfs.

4.2. *Fits of the Entire SED*

We fit the 0.95–14.5 μm spectrum of each dwarf as described in the previous section. Although the data extend blueward to 0.65 μm, the analysis was limited to wavelengths greater than 0.95 μm because the pressure-broadened wing of the resonant K I doublet ($\lambda\lambda$7665, 7699) that extends to $\sim$0.9 μm is exceedingly difficult to model (Burrows & Volobuyev 2003). Table 3 lists the best-fitting model parameters ($T_{\rm eff}$, log g, $f_{\rm sed}$) for each dwarf in our sample, along with the fraction of the Monte Carlo simulations ($f_{\rm MC}$) in which the given triplet was identified as the best-fitting model. All models with $f_{\rm MC} > 0.1$ are listed. A summary of the derived parameters is shown in Figure 5. Seven of the nine dwarfs in our sample have best-fitting synthetic spectra with $f_{\rm MC} \sim 1$, indicating that they are the only reasonable model spectra in our grid for these dwarfs. There are two model spectra for 2MASS 1439+1929 (L1) that differ by 1 in $f_{\rm sed}$ with nearly equal $f_{\rm MC}$ values, while SDSS 1254−0122 (T2) has two models with $f_{\rm MC} > 0.1$ that differ by 0.5 dex in log g and 1 in $f_{\rm sed}$.

[13] The χ^2 distribution with ν degrees of freedom is defined as the sum of ν^2 standard normal deviates or $\chi^2_\nu = \sum z_i^2$, where $z_i = (x_i - \mu)/\sigma_i$. Since the models are known to have systematic errors, the standardized residuals $z_i = (f_i - C_k \mathcal{F}_{k,i})/\sigma_i$ are not standard normal deviates; thus, G does not follow a χ^2 distribution.

TABLE 3
Derived Parameters for L and T Dwarfs (0.9–14.5 μm)

Object	Spectral Type[a]		Atmospheric Parameters					Golimowski et al. $T_{\rm eff}$ (K)		
			By Spectral Fitting				By Evolutionary Sequences			
	Optical	Infrared	$T_{\rm eff}$ (K)	$\log g$ (cm s^{-2})	$f_{\rm sed}$	$f_{\rm MC}$	$\log g$ (cm s^{-2})	0.1 Gyr	3 Gyr	10 Gyr
2MASS J1439+1929	L1	L1	2100	5.0	2	0.582	5.1	1950	2250	2275
	...	...	2100	5.0	3	0.418	5.1	1950	2250	2275
2MASS J1506+1321	L3	...	1800	4.5	1	1.000	...	...	...	...
2MASS J0036+1821	L3.5	L4 ± 1	1700	5.5	3	1.000	4.9	1650	1900	1975
2MASS J2224−0158	L4.5	L3.5	1700	4.5	1	0.999	5.3	1475	1750	1800
2MASS J1507−1627	L5	L5.5	1700	4.5	2	1.000	5.4	1475	1750	1800
2MASS J0825+2115	L7.5	L6	1400	4.5	1	1.000	5.4	1175	1425	1475
DENIS 0255−4700	L8	L9	1400	5.5	2	0.988	5.5	1150[b]	1375	1425
SDSS J1254−0122	T2	T2	1200	5.0	3	0.831	4.7	1150	1425	1500
	...	...	1200	5.5	2	0.105	4.9	1150	1425	1500
2MASS J0559−1404	T5	T4.5	1200	5.5	4	0.999	4.7	1150	1425	1500

Note.—Only models with $f_{\rm MC} > 0.1$ are listed.
[a] Spectral types of the L dwarfs are from Kirkpatrick et al. (1999, 2000), Reid et al. (2000), Gizis et al. (2000), Geballe et al. (2002), Knapp et al. (2004), Burgasser et al. (2006b), and J. D. Kirkpatrick (in preparation). Spectral types of the T dwarfs are from Burgasser et al. (2003a, 2006b). Errors on spectral types are ±0.5 subclass unless otherwise noted.
[b] DENIS 0255−4700 was not included in the Golimowski et al. (2004) sample. We have computed its $L_{\rm bol}$ using the new parallax measurement of Costa et al. (2006). The bolometric flux was determined by integrating over its 0.6–14.5 μm spectrum as described in Cushing et al. (2006).

The derived $T_{\rm eff}$ values decrease steadily with later spectral type, but the difference in $T_{\rm eff}$ between 2MASS 0825+2115 (L7.5) and 2MASS 0559−1404 (T4.5) is only 200 K, which confirms that the transition between the L and T dwarfs occurs over a narrow range in $T_{\rm eff}$, as has been noted previously (e.g., Kirkpatrick et al. 1999; Burgasser et al. 2002b; Golimowski et al. 2004). Golimowski et al. (2004) derive the effective temperatures of ∼40 L and T dwarfs using their observed bolometric luminosities and evolutionary models (see Dahn et al. [2002], Vrba et al. [2004], and Basri et al. [2000] for alternative $T_{\rm eff}$ scales for L and T dwarfs). Seven of these dwarfs are included in our sample, so we also show in Table 3 the Golimowski et al. $T_{\rm eff}$ values for ages of 0.1, 3, and 10 Gyr. The agreement between the two sets of values is excellent, as all of our derived values fall within their 0.1–10 Gyr ranges.

The comparison of our derived $T_{\rm eff}$ values with those of Golimowski et al. (2004) implies that if they are single objects, seven of the nine dwarfs in our sample are much younger than 3 Gyr. Our evolutionary calculations (M. S. Marley et al. 2008, in preparation) also indicate that if we take the derived $T_{\rm eff}$ and g values at face value, five of the L dwarfs would be younger than 0.2 Gyr. This is primarily a consequence of the low gravities obtained from fitting the SEDs. It seems unlikely that our sample would be biased toward such young ages, given that the mean age of the L and T dwarf field population is several gigayears (Dahn et al. 2002; Allen et al. 2005). This suggests that fitting the SEDs of ultracool dwarfs is a poor method of determining gravities. Fortunately, we can obtain the gravity using an alternate method.

When the parallax of an object is known, its radius can be determined using the fitted normalization constant (eq. [2]), since $C_k = (R/d)^2$. With ultracool dwarf evolution sequences, ($T_{\rm eff}$, R) values can be transformed uniquely into ($T_{\rm eff}$, g) values. The gravities obtained with this alternate method are given in Table 3 and are shown in green in Figure 5 (*top*). The scatter in $\log g$ is reduced, and nearly all gravities are above $\log g = 5.0$. Our evolution sequences show that all nine objects now have ages above 0.3 Gyr. This alternate method only weakly depends on the relatively subtle variations in spectral morphology arising from changes in g (Figs. 2 and 3) because it relies primarily on fitting the absolute flux level of the SED. The reduced scatter in $\log g$ and the older age distribution of our sample indicate that the method provides gravity estimates that are more reliable than those obtained by direct spectral fitting. Hereafter, we do not compute new model atmospheres with these new gravities but rather continue to compare the data to models in our grid with $\log g = 4.5$, 5.0, and 5.5.

We also note that the theoretical evolution of ultracool dwarfs with cloudy atmospheres is limited to $\log g \leq 5.38$, although the evolution with cloudless atmospheres can reach slightly higher gravities of $\log g \sim 5.48$. Because the mass-$T_{\rm eff}$-radius relation of brown dwarfs is well established on theoretical grounds, it provides a firm boundary to physically plausible combinations of $T_{\rm eff}$ and g. We find that the $\log g$ values of three of our objects (derived using the alternate method) exceed the limit for ultracool dwarfs with cloudy atmospheres, which is an indication that their fitted $T_{\rm eff}$ values are overestimated by ∼10–20 K. This result can be understood by noting that the gravity of brown dwarfs is a very sensitive function of $T_{\rm eff}$ for a fixed $L_{\rm bol}$ (see, e.g., Fig. 1 of Saumon et al. 2006). This is a consequence of the mass-radius relation for degenerate stars, where $R \sim M^{-1/3}$. Since $L_{\rm bol} \sim R^2 T_{\rm eff}^4$, it follows that at constant $L_{\rm bol}$, $g \sim T_{\rm eff}^{10}$. From this approximate relation, a 7% variation in $T_{\rm eff}$ changes the gravity by 0.3 dex.

Two objects in our sample call for a more detailed discussion. SDSS 1254−0122 (T2) and especially 2MASS 0559−1404 (T4.5) stand out as being overluminous for their spectral types (Burgasser 2007). It has therefore been suggested that the two objects may be unresolved binaries (Golimowski et al. 2004; Vrba et al. 2004; Liu et al. 2006; Burgasser 2007), although neither dwarf has been resolved into a binary in high-resolution imaging (Burgasser et al. 2003b, 2006c). We find, as did Golimowski et al. (2004), that the two objects share essentially the same $T_{\rm eff}$, although we derive $T_{\rm eff} = 1200$ K while Golimowski et al. find $T_{\rm eff} = 1475$ K (assuming ages of 3 Gyr). If SDSS 1254−0122 and 2MASS 0559−1404 are equal-magnitude binaries, then the $L_{\rm bol}$ of each component is reduced by a factor of 2, and the Golimowski et al. $T_{\rm eff}$ value becomes ∼1200 K, which is in much better agreement with our value. Given these new parameters, our evolutionary sequences provide the corresponding properties for the individual

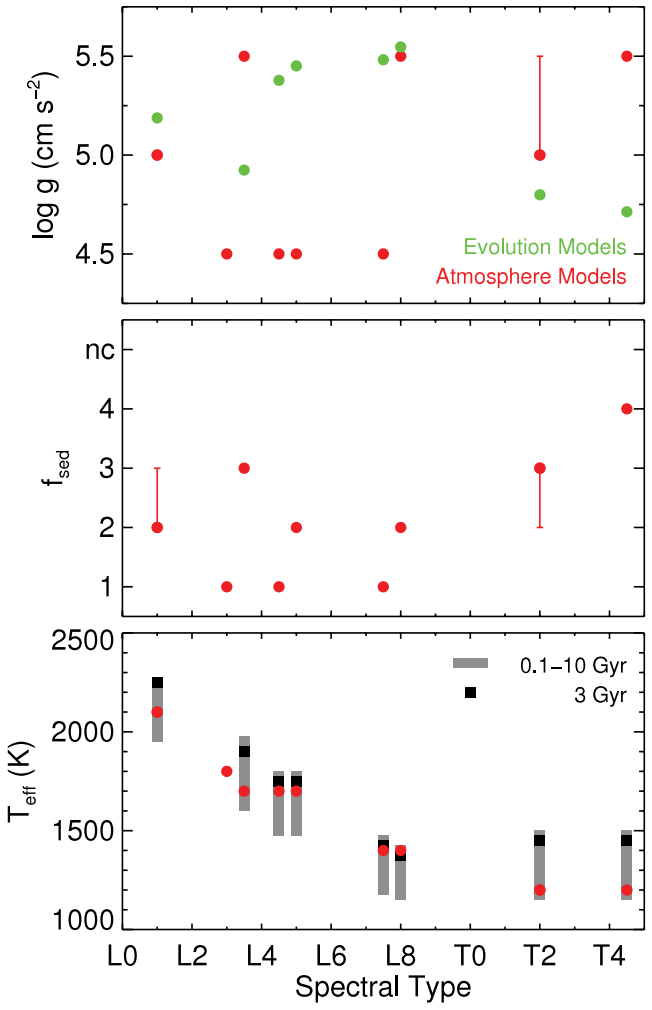

FIG. 5.—Summary of the best-fitting model triplet ($T_{\rm eff}$/log g/$f_{\rm sed}$) values over the 0.95–14.5 μm wavelength range for each dwarf in our sample (*red circles*). Error bars denote the range of parameters for the models with $f_{\rm MC} > 0.1$. In the top panel, the green circles are the log g values derived using evolutionary models. In the bottom panel, the gray regions denote the $T_{\rm eff}$ range corresponding to an age range of 0.1–10 Gyr, and the black squares denote the $T_{\rm eff}$ corresponding to 3 Gyr (Golimowski et al. 2004). All of the $T_{\rm eff}$ determinations fall within the 0.1–10 Gyr $T_{\rm eff}$ range. 2MASS 1506+1321 (L3) lacks a parallax and therefore does not have a $T_{\rm eff}$ range plotted.

components. To satisfy both the constraints of component luminosity and the maximum allowed gravity, $T_{\rm eff}$ has to be reduced slightly but remain within the uncertainties of our spectral fits. The properties of the individual components are given in Table 4.

Whether SDSS 1254−0122 and 2MASS 0559−1404 are singles or equal-mass binaries, they have essentially the same effective temperature. The difference in the appearance of their spectra (T2 vs. T4.5) can be explained as primarily due to a difference in their cloud properties, as suggested by our fits that indicate the clouds are thinner (larger $f_{\rm sed}$) in 2MASS 0559−1404 than in SDSS 1254−0122. Another possibility would be for SDSS 1254−0122 to be a single brown dwarf (or a strongly unequal-mass binary) and for 2MASS 0559−1404 to be an equal-mass binary. This would make the latter's individual components less luminous than SDSS 1254−0122 (or its primary) and is consistent with their position in the $M_{\rm bol}$ versus spectral type diagram (Burgasser 2007).

A fair amount of scatter is found in the $f_{\rm sed}$ values of the L dwarfs, with an indication that $f_{\rm sed}$ increases toward the later T spectral class, as would be expected if clouds play a decreasing role in shaping the SED of T dwarfs (e.g., Marley et al. 2002; Burrows et al. 2006). Among the L dwarfs in our sample, $f_{\rm sed}$ ranges from 1 to 3, implying that cloud opacity varies appreciably among L dwarfs (Fig. 2, *bottom*) with little, if any, dependence on spectral type. It would be particularly interesting to establish the distribution of $f_{\rm sed}$ as a function of spectral type with a larger sample.

Figure 6 shows the 0.95–14.5 μm spectra of 2MASS 1439+1929 (L1), 2MASS 0036+1821 (L3.5), 2MASS 1507−1627 (L5), DENIS 0255−4700 (L8), SDSS J1254−0122 (T2), and 2MASS 0559−1404 (T4.5), along with the best-fitting model spectra. The gray regions indicate wavelength ranges that were excluded from the fits. The models fit the data reasonably well at the earliest and latest spectral types, but they do a poorer job of fitting the data in the mid- to late-type L dwarfs and the early-type T dwarf. This range of spectral types corresponds to the L/T transition, where condensate clouds have their largest impact on the SED of ultracool dwarfs. The relatively poor fits at the L/T transition most likely reflect the limitations of our simple cloud model.

In particular, the best-fitting model spectra match both the peaks and depths of the H_2O bands centered at 1.4, 1.9, and 2.6 μm well. The models do, however, underestimate the K-band flux density levels of 2MASS 1439+1929 (L1) and 2MASS 0036+1821 (L3.5). In addition, the models also overestimate the depth of the L-band CH_4 absorption bands of both DENIS 0255−4700 (L8) and SDSS 1254−0122 (T2), as well as the 5.5–14.5 μm flux levels of DENIS 0255−4700 (L8). We defer discussion of the possible causes of these mismatches to § 4.3. Finally, the poor match between the model spectrum and data of 2MASS 0559−1404 in the H band is a result of the woefully incomplete line list of CH_4 at these wavelengths (Burrows et al. 2001; Freedman et al. 2008).

4.3. *Description of Individual Bands*

In the following sections, we describe how well the best-fitting synthetic spectra match the data over narrower wavelength ranges. Figures 7–12 show the same data and model spectra presented in Figure 6 but over the wavelengths covered by the photometric bandpasses Y, J, H, K, and L and the Short-Low module of the IRS on board *Spitzer* (hereafter IRS/SL). Although the most

TABLE 4
THE PROPERTIES OF SDSS 1254−0122 AND 2MASS 0559−1404

	SDSS 1254−0122		2MASS 0559−1404	
PARAMETER	Single	Equal-Mass Binary	Single	Equal-Mass Binary
log ($L_{\rm bol}/L_\odot$)	−4.60	−4.90	−4.63	−4.93
$T_{\rm eff}$ (K)	1200	<1160	1200	<1150
log g (cm s^{-2})	4.71	<5.38	4.80	<5.38
Age (Gyr)	~0.3	<10	~0.4	<10

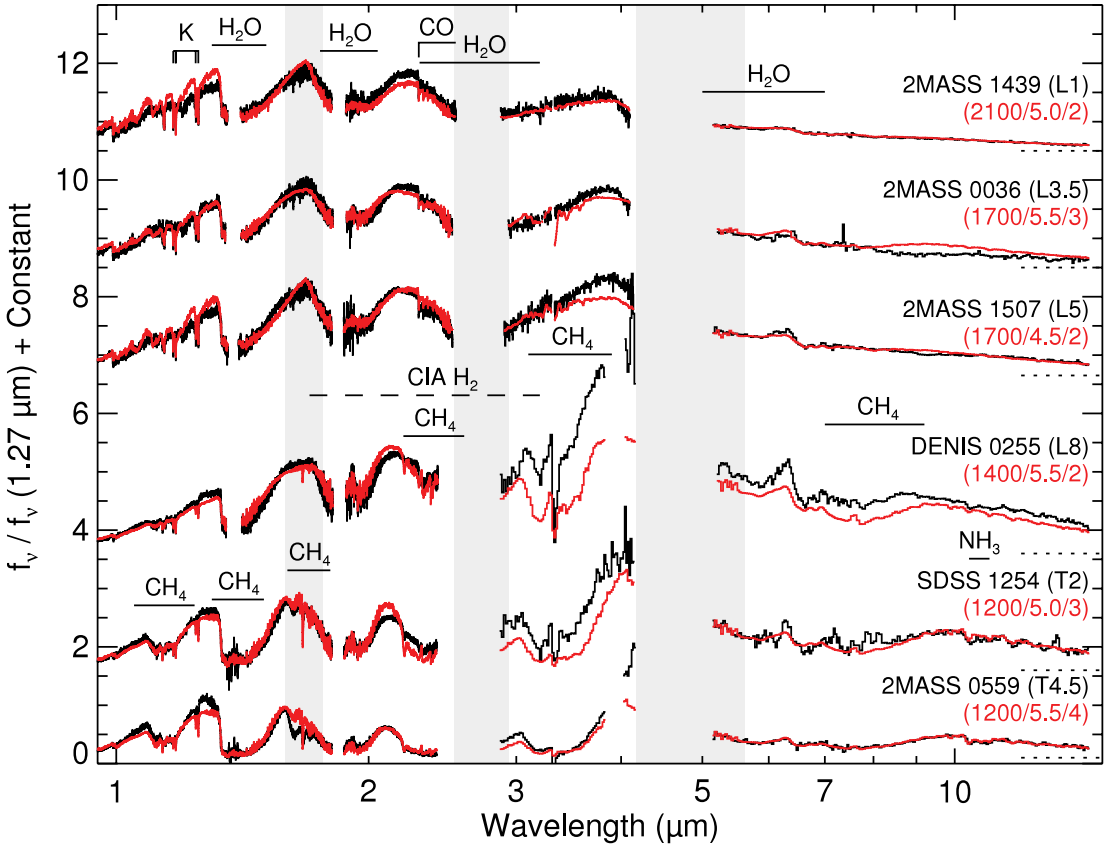

FIG. 6.—The 0.95–14.5 μm spectra of 2MASS 1439+1929 (L1), 2MASS 0036+1821 (L3.5), 2MASS 1507−1627 (L5), DENIS 0255−4700 (L8), SDSS 1254−0122 (T2), and 2MASS 0559−1404 (T4.5) (*black lines*). The data have been normalized to unity at 1.27 μm and offset (*dotted lines*) for clarity. The best-fitting models ($T_{\rm eff}$/ log g/$f_{\rm sed}$) are shown in red and have been normalized and offset with the same constants as the data. The models were multiplied by the constant C (see § 4.1) before normalization to preserve the relative flux levels between the data and models. Regions not included in the fits are shown in light gray.

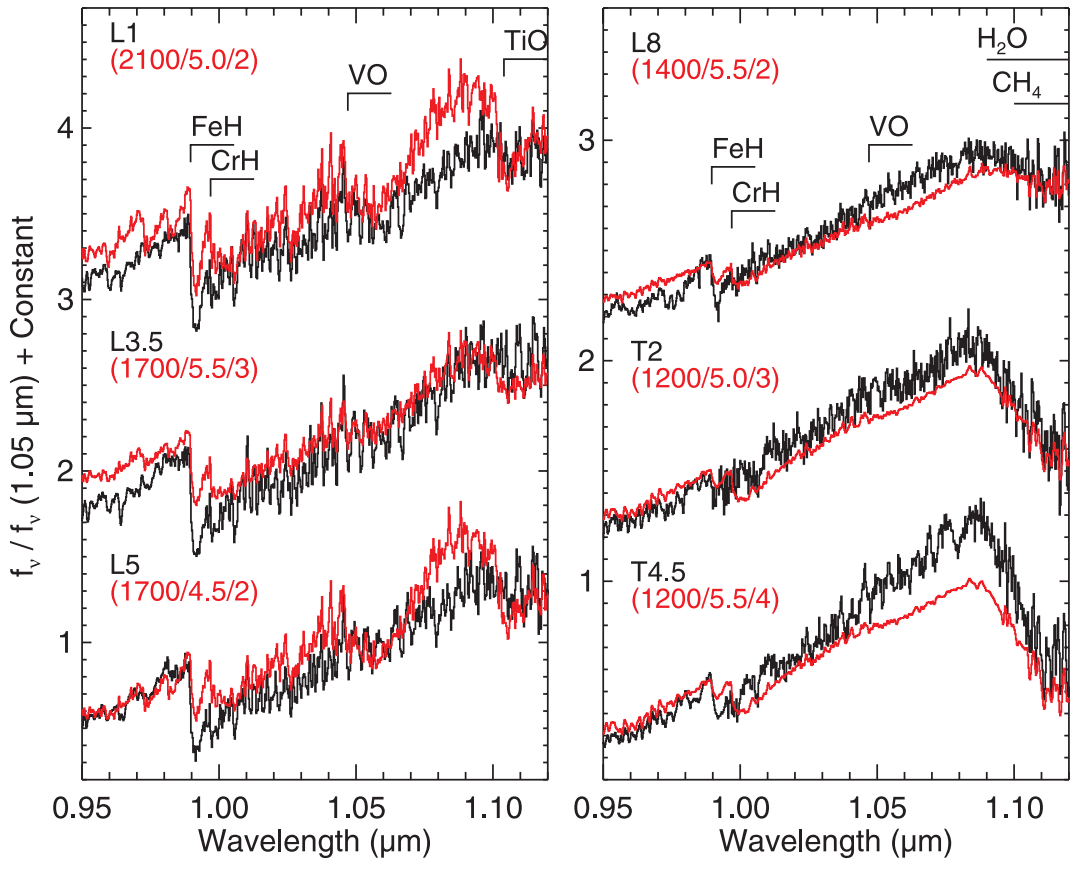

FIG. 7.—Same as Fig. 6, except the data cover the Y band and were normalized at 1.05 μm.

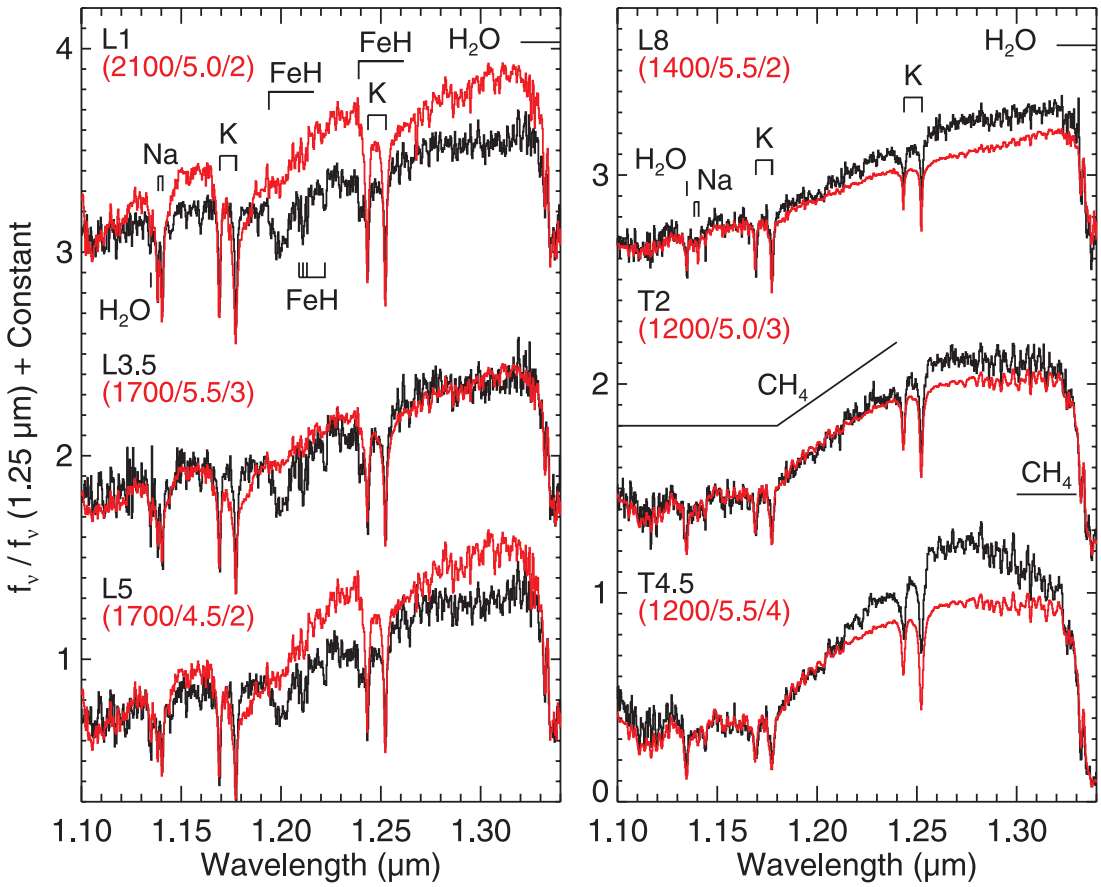

FIG. 8.—Same as Fig. 6, except the data cover the *J* band and were normalized at 1.25 μm.

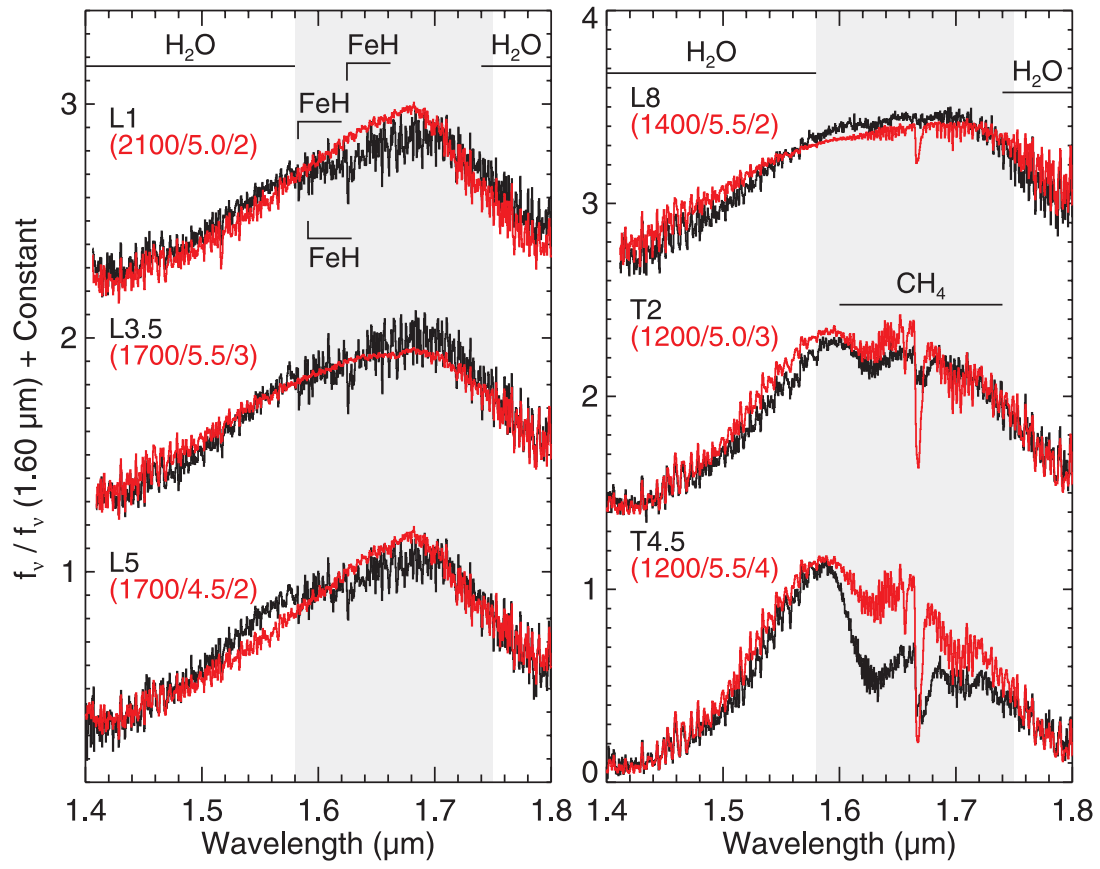

FIG. 9.—Same as Fig. 6, except the data cover the *H* band and were normalized at 1.6 μm.

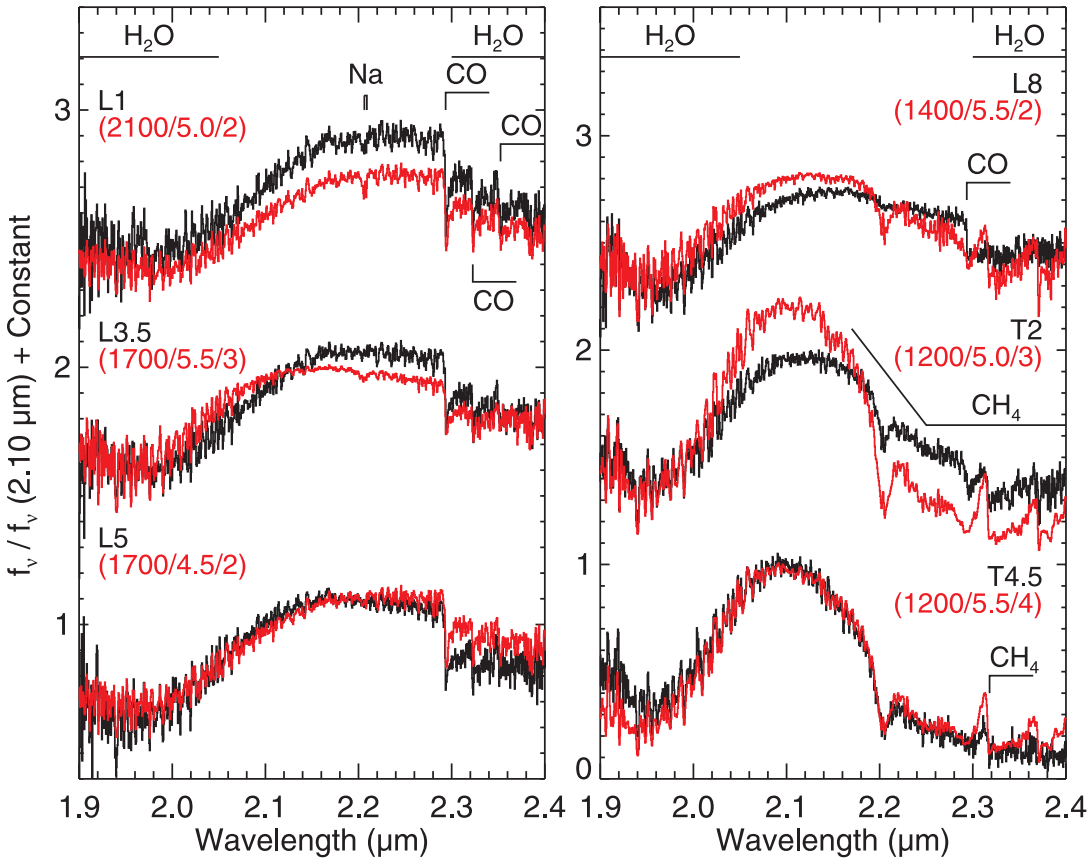

FIG. 10.—Same as Fig. 6, except the data cover the *K* band and were normalized at 2.1 μm.

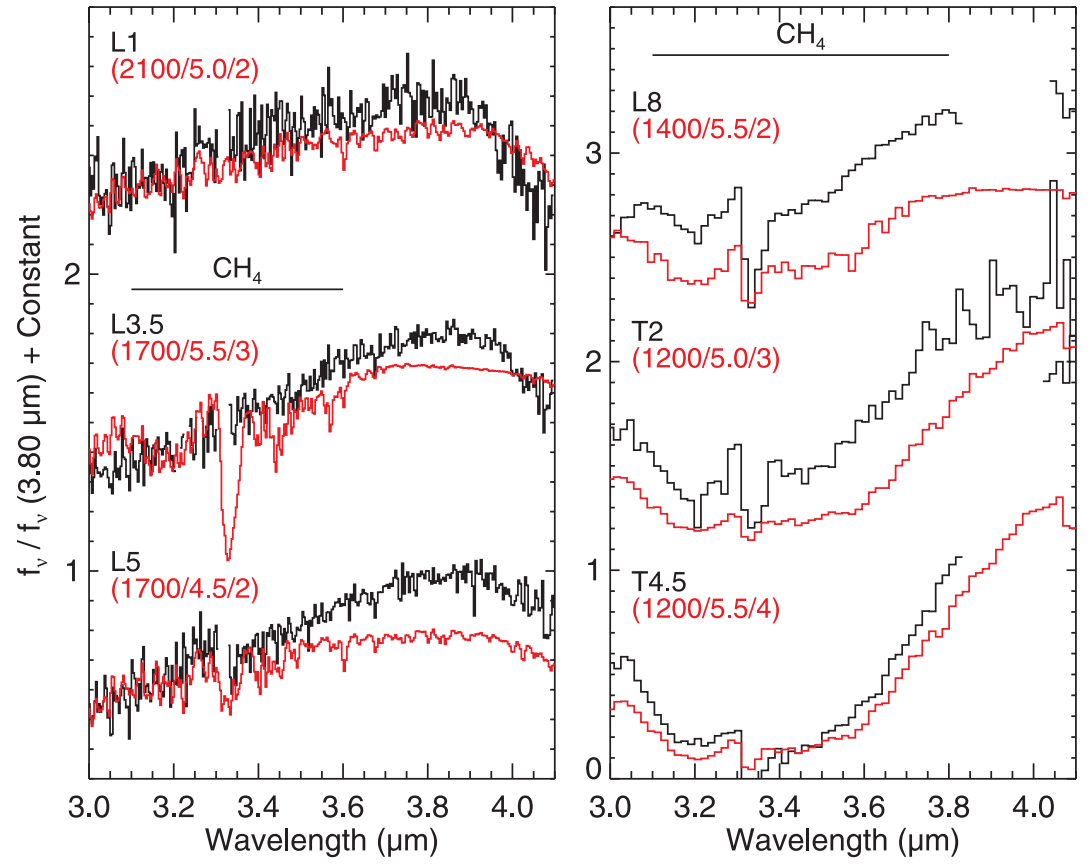

FIG. 11.—Same as Fig. 6, except the data cover the *L* band and were normalized at 3.8 μm.

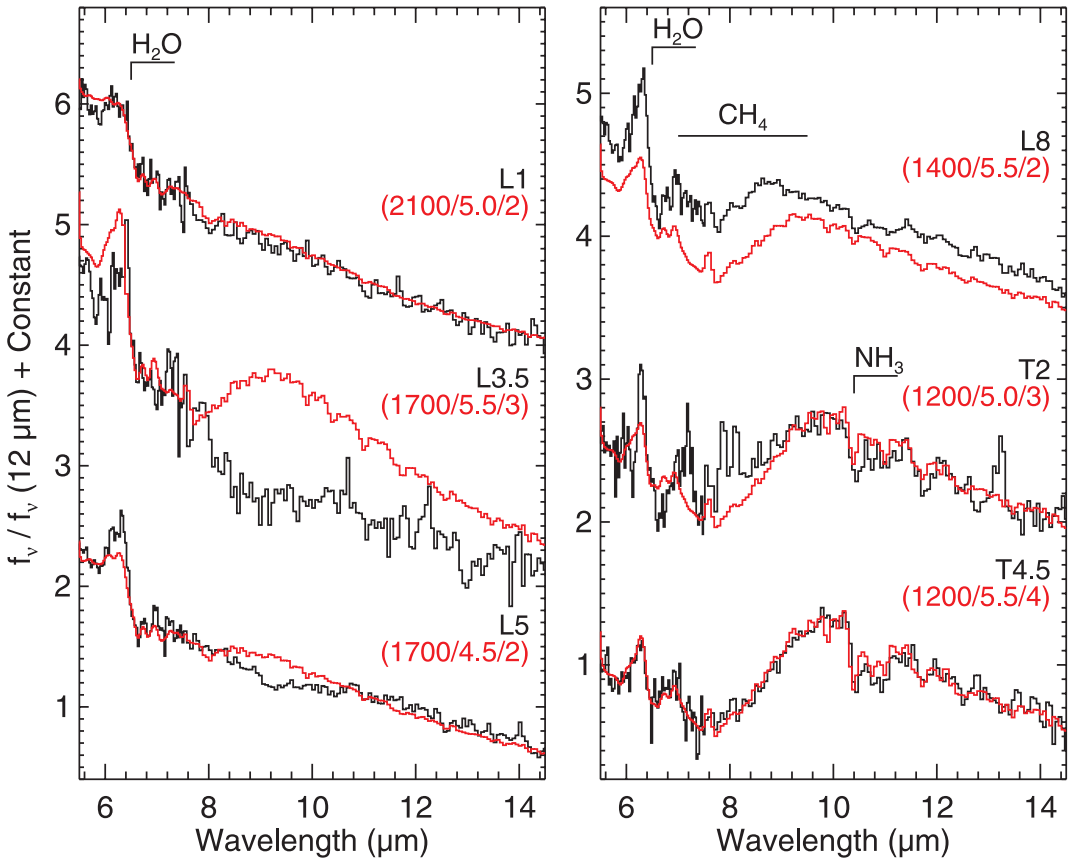

FIG. 12.—Same as Fig. 6, except the data cover the IRS/SL wavelength range and were normalized at 12 μm.

prominent features in the spectra of the L and T dwarfs are briefly described in each section, more detailed descriptions can be found elsewhere (Kirkpatrick et al. 1999; Burgasser et al. 2003a; McLean et al. 2003; Cushing et al. 2005, 2006).

4.3.1. *The Y Band*

Figure 7 shows the spectra and best-fitting models over the wavelength range 0.95–1.1 μm, which roughly corresponds to the Y band (Hillenbrand et al. 2002). The spectra of the L dwarfs are dominated by absorption features arising from the 0–0 band of the $F^4\Delta - X^4\Delta$ system of FeH. The strongest FeH feature is the band head at 0.9896 μm, but weak FeH features are seen in the spectra of the L dwarfs throughout this wavelength range. The 0–0 band of the $A^4\Pi - X^4\Sigma^-$ system of VO centered at $\sim$1.06 μm is also present in the spectra of the early-type L dwarfs, and the FeH band head at 0.9896 μm is weakly present in the spectra of SDSS J1254−0122 (T2) and 2MASS 0559−1404 (T4.5). Finally, H_2O and CH_4 bands at $\lambda > 1.09$ μm emerge at the L/T transition and strengthen through the T sequence.

The synthetic spectra fit the overall shape of the Y-band spectra of the L and T dwarfs reasonably well. In particular, they match the strengths of the H_2O and CH_4 bands in the T dwarf spectra at $\lambda > 1.08$ μm. However, there are a number of mismatches worth noting. First, the FeH band head in the synthetic spectra is systematically weaker than in the L dwarf data. Second, all of the synthetic spectra exhibit the 0–1 band head of the $A^6\Sigma^+ - X^6\Sigma^+$ system of CrH at 0.9969 μm. This band head is often identified in the spectra of L dwarfs (e.g., Kirkpatrick et al. 1999; Kendall et al. 2007), but Cushing et al. (2003) questioned these identifications, given that many of the absorption features at this wavelength in $R = 2000$ spectra can be associated with FeH. Reiners & Basri (2006) recently found that no CrH absorption features can be identified in high-resolution ($R = 31{,}000$) spectra of M and L dwarfs, which indicates that CrH is not a significant absorber at these wavelengths. Therefore, the presence of this band head in the synthetic spectra is inconsistent with the observations. The 0–1 band head of the ϕ system of TiO (Galehouse et al. 1980) at $\sim$1.104 μm is also too strong in all of the model spectra. The T dwarf models exhibit a broad, weak VO band centered at $\sim$1.06 μm. Observationally, this band peaks in strength at a spectral type of $\sim$L5 and is absent by a spectral type of L8 (Cushing et al. 2005), so the presence of this band in the models is also inconsistent with the observations. Finally, the best-fitting model spectrum underestimates the peak flux of the T4.5 dwarf 2MASS 0559−1404 because of the presence of the condensate opacity ($f_{\rm sed} = 4$). A cloudless model would match the overall shape of the Y band better (see § 4.4.1).

4.3.2. *The J Band*

Figure 8 shows the spectra and best-fitting model spectra from 1.1 to 1.34 μm. This wavelength range contains the most prominent atomic features in the infrared spectra of L and T dwarfs, namely, the two K I doublets at $\sim$1.17 and $\sim$1.24 μm and the Na I doublet at 1.14 μm. The 0–1 and 1–2 bands of the $F^4\Delta - X^4\Delta$ system of FeH are also present in the J-band spectra of the L dwarfs. These two bands exhibit band heads at 1.1939 and 1.2389 μm, respectively, along with numerous additional weak features from 1.2 to 1.3 μm. The $3\nu_3$ and $\nu_2 + 2\nu_3$ bands of CH_4 centered at $\sim$1.15 and $\sim$1.4 μm are also seen in the spectra of the T dwarfs.

The model spectra reproduce the depths of the H_2O bands at $\lambda > 1.32$ μm, the onset of the CH_4 absorption in the spectra of the T dwarfs, and the weakening and eventual disappearance of

the Na I doublet at 1.14 μm with later spectral type. However, the model spectra do a poor job of matching the peak flux levels at $\sim$1.3 μm of 2MASS 1439+1929 (L1), 2MASS 1507−1627 (L5), and 2MASS 0559−1404 (T4.5). In addition, the band heads and other weak FeH features observed in the *J*-band spectra of the L dwarfs are completely absent from the models. This behavior mirrors that in the *Y* band for which the FeH band is systematically weaker in the models than in the data. The cross sections of the 0–1 and 1–2 μm FeH bands are an order of magnitude smaller than those of the 0–0 FeH band (Dulick et al. 2003), so it is not surprising that they are either very weak or absent in the synthetic spectra.

The models also are a poor match to the early-type L dwarfs near the 1.177 μm K I line, since the red wing appears much too broad given the observations. This apparent line broadening in the model spectra is actually due to the presence of the 0–1 band of the $A^4\Pi - X^4\Sigma^-$ system of VO (Cheung et al. 1982). Although this band has been identified in the spectra of young, low-gravity brown dwarfs (McGovern et al. 2004), it has not been found in the spectra of field L and T dwarfs; therefore, its presence in the model spectrum implies that the opacity of this VO band may be in error.

4.3.3. *The H Band*

Figure 9 shows the spectra and best-fitting synthetic spectra over the 1.4–1.8 μm wavelength range. The L dwarf spectra are shaped primarily by H_2O absorption but also exhibit numerous weak absorption features, including three band heads from 1.59 to 1.74 μm that arise from the $E^4\Pi - A^4\Pi$ system of FeH. The $2\nu_3$ and $2\nu_2 + \nu_3$ bands of CH_4 appear at the L/T transition and strengthen through the T sequence. As explained in § 4.1, we do not include the 1.58–1.75 μm wavelength range in the fits because the FeH band lacks a line list and the CH_4 line list is incomplete.

The model spectra fit the overall shape of the data reasonably well at these wavelengths. In particular, the detailed structure of the H_2O bands at the short- and long-wavelength ends of the *H* band are well matched by the model spectra. The best agreement between the data and model spectra at these wavelengths is obtained for DENIS 0255−4700 (L8) and SDSS 1254−0122 (T2) because the FeH band is either weak or absent from the data and only weak CH_4 absorption is present. This indicates that the H_2O opacity tables are quite good in the *H* band.

4.3.4. *The K Band*

Figure 10 shows the data and best-fitting synthetic spectra over the 1.9–2.4 μm wavelength range. The spectra of L and T dwarfs are shaped primarily by H_2O, CO, and CH_4 bands at these wavelengths. At the earliest spectral types, CO is the dominant carbon-bearing gas; therefore, the $\Delta\nu = +2$ CO overtone bands at $\lambda \gtrsim 2.29$ μm are strong. These CO bands weaken and disappear with later spectral type as CH_4 becomes the dominant carbon-bearing gas. In addition, there is a Na I doublet at 2.26 μm present in the early-type L dwarfs.

With the exception of 2MASS 1507−1627 (L5) and 2MASS 0559−1404 (T4.5), the models are a poor fit to the *K*-band spectra. The models underestimate the *K*-band flux levels of 2MASS J1439+1929 (L1) and 2MASS 0036+1821 (L3.5) and overestimate the strengths of the CH_4 band in DENIS 0255−4700 (L8) and SDSS J1254−0122 (T2). In addition, a weak CH_4 feature can be seen in the synthetic spectrum of 2MASS 0036+1821 (L3.5) at $\sim$2.2 μm that is not observed in spectra of ultracool dwarfs until a spectral type of $\sim$L8. The presence of this CH_4 feature in the model spectrum of 2MASS 0036+1821 is a result of the fact that $f_{sed} = 3$ for this model. For a comparison, the best-fitting model for 2MASS 1507−1627 (L5) has the same T_{eff} but $f_{sed} = 2$ and shows no CH_4 feature (the change in *g* makes little difference in the strength of the CH_4 band at this T_{eff}). The $f_{sed} = 3$ model is cooler in the CH_4 band formation region, resulting in a higher CH_4 abundance and a deeper absorption band.

As described in § 3, H_2 CIA is an important pressure-sensitive opacity source in the atmospheres of ultracool dwarfs. Compared to the absorption of other molecules, primarily H_2O and CH_4, H_2 CIA is most significant in the *K* band. A lower metallicity decreases the opacity of H_2O and CH_4 relative to the H_2 CIA continuum, which results in stronger emission in the *Y*, *J*, and *H* bands with respect to the *K* band (Burgasser et al. 2002b). In previous work (Saumon et al. 2006, 2007) we found that our solar metallicity models systematically underestimated the *K*-band fluxes of late-type T dwarfs, while models with [Fe/H] = +0.3 fit the *K*-band peak well. Therefore, the poor match between the data and model spectra in the *K* band may indicate that the metallicities of the L and T dwarfs in our sample differ somewhat from the solar value employed in our chemical equilibrium calculations. Another possibility that explains the mismatch between the spectra of DENIS 0255−4700 (L8) and SDSS 1254−0122 (T2) and the best-fitting models is the cloud properties, since the cloud sedimentation efficiency f_{sed} changes from 2 to 3 to 4 from L8 to T4.5.

4.3.5. *The L Band*

Figure 11 shows the spectra and best-fitting synthetic spectra over the 3.0–4.1 μm wavelength range. The spectra are dominated by weak H_2O features and the ν_3 fundamental band of CH_4. The *Q*-branch ($\sim$3.3 μm) is the first CH_4 feature to emerge in the spectra of the L dwarfs and does so at a spectral type of $\sim$L5. With increasing spectral type, the *P*- and *R*-branches emerge and strengthen through the spectral sequence until the band is saturated in the late-type T dwarfs.

The model spectra do not match the data particularly well in the *L* band. The most egregious mismatch is 2MASS 0036+1821 (L3.5), for which the model shows a very strong CH_4 band that is absent in the data. The presence of the CH_4 band is due to the fact that the best-fitting model has $f_{sed} = 3$, as in the *K* band (see § 4.3.5). The average flux density levels of the models also appear low for 2MASS 1507−1627 (L5), DENIS 0255−4700 (L8), SDSS J1254−0122 (T2), and 2MASS 0559−1404 (T4.5). In addition, the model for 2MASS J0559−1404 does not match the peak of the observed spectrum at $\sim$4.1 μm. Generally, in objects where the CH_4 absorption is too strong in the *L* band, a corresponding mismatch occurs in the *K* and IRS/SL bands (L8 and T2). The line lists for both H_2O and CH_4 are reasonably complete at these wavelengths, so the most likely explanation for the mismatch is that the region of the model atmosphere from which the *K*- and *L*-band and IRS/SL flux emerges is too cool, possibly as a result of the condensate cloud model.

4.3.6. *IRS/SL*

Figure 12 shows the data and best-fitting models over the 5.5–14.5 μm wavelength range covered by the Short Low module of the IRS (Houck et al. 2004). H_2O absorption features arising from the ν_2 fundamental band and $2\nu_2$–ν_2 overtone band are present throughout this wavelength range; the break in the spectra at 6.5 μm is an H_2O feature. The ν_4 fundamental band of CH_4 centered at $\sim$7.65 μm emerges in the spectra of late-type L dwarfs, and the ν_2 fundamental band of NH_3 centered at $\sim$10.5 μm appears in the spectra of the T dwarfs.

With the exception of 2MASS 0036+1821 (L3.5), the synthetic spectra match the data reasonably well. In particular, the strengths of the H_2O band at 6.5 μm and the CH_4 band at 7.8 μm

TABLE 5
Derived Parameters of L and T Dwarfs from Restricted Spectral Intervals

Object	Spectral Type[a]		$T_{\rm eff}$ (K)/log g (cm s^{-2})/$f_{\rm sed}$/$f_{\rm MC}$					
	Optical	Infrared	Y	J	K	L	IRS/SL	Near-Infrared
2MASS 1439+1929.....	L1	L1	1700/5.5/3/1.000	2400/4.5/1/1.000	2100/5.0/3/1.000	2400/5.5/2/0.922	2200/5.5/3/0.922	1800/5.0/3/1.000
2MASS 1506+1321.....	L3	...	1800/5.5/4/1.000	1500/5.5/1/1.000	1900/4.5/3/0.761	2400/5.5/4/0.997	2400/5.5/1/1.000	1600/4.5/2/1.000
	...	...	...	...	1900/4.5/2/0.240	...	...	...
2MASS 0036+1821.....	L3.5	L4 ± 1	1700/5.5/4/0.988	1700/5.5/2/1.000	2000/5.0/4/1.000	2300/5.5/nc/1.000	2400/5.5/1/0.863	1700/5.5/3/1.000
2MASS 2224−0158	L4.5	L3.5	1600/5.5/3/0.996	1500/5.0/1/1.000	2400/5.5/nc/0.748	1900/4.5/4/0.219	2400/5.5/1/1.000	1400/4.5/1/1.000
	...	...	...	...	2300/5.0/nc/0.133	2200/5.5/nc/0.190	...	...
	...	...	...	...	...	2300/5.5/nc/0.122	...	...
	...	...	...	...	...	1800/5.0/4/0.114	...	...
2MASS 1507−1627	L5	L5.5	1600/5.5/3/1.000	1500/5.5/2/0.999	1700/5.0/3/1.000	2300/5.5/nc/1.000	1900/5.0/3/0.627	1700/5.5/3/1.000
	...	...	...	...	...	...	2000/5.0/3/0.370	...
2MASS 0825+2115	L7.5	L6	1400/5.5/2/0.549	1300/4.5/1/0.984	1500/4.5/2/0.835	1800/5.0/4/0.998	2400/5.5/nc/0.201	1400/4.5/1/1.000
	...	...	1500/5.0/2/0.359	...	1700/5.0/3/0.166	...	2200/5.5/4/0.166	...
	...	...	...	...	...	...	2300/5.5/nc/0.157	...
	...	...	...	...	...	...	1900/5.5/4/0.142	...
DENIS 0255−4700	L8	L9	1300/5.5/2/0.992	1300/5.5/2/0.999	1700/5.5/4/0.820	1900/5.5/nc/0.447	1200/5.5/1/0.465	1500/4.5/2/0.572
	...	...	...	...	1800/5.5/4/0.177	1700/5.5/4/0.241	1500/4.5/2/0.218	1400/4.5/2/0.428
	...	...	...	...	...	1700/5.0/4/0.186	1200/5.0/1/0.167	...
SDSS 1254−0122.....	T2	T2	1000/4.5/2/1.000	1200/4.5/3/1.000	1500/5.5/4/1.000	1500/5.5/3/0.918	1400/5.5/nc/0.910	1400/4.5/4/1.000
2MASS 0559−1404	T4.5	T4.5	1200/5.5/nc/1.000	1100/4.5/4/1.000	1100/4.5/2/1.000	1100/4.5/nc/0.469	1200/5.5/4/0.982	1100/5.0/4/1.000
	...	...	...	...	...	1000/4.5/3/0.366	...	...

Note.—Only models with $f_{\rm MC} > 0.1$ are listed.
[a] Spectral types of the L dwarfs are from Kirkpatrick et al. (1999, 2000), Reid et al. (2000), Gizis et al. (2000), Geballe et al. (2002), Knapp et al. (2004), Burgasser et al. (2006b), and J. D. Kirkpatrick (in preparation). Spectral types of the T dwarfs are from Burgasser et al. (2003a, 2006b). Errors on spectral types are ±0.5 subclass unless otherwise noted.

are well matched by the model spectra. The flux level of the synthetic spectrum of DENIS 0255−4700 (L8) is low, however, and there is a slight mismatch between the model spectrum and 2MASS 1507−1627 (L5) at ∼9 μm that we discuss further in § 4.4.5. The mismatch between the model and the spectrum of 2MASS 0036+1821 is due to the fact that the model has $f_{\rm sed} = 3$ (see §§ 4.3.4 and 4.3.5).

4.4. *Fits to Individual Photometric Bands*

The L and T dwarf spectra studied herein cover a broad range of wavelengths, while most published spectra cover only the red optical and near-infrared wavelengths (e.g., Cruz et al. 2003; Knapp et al. 2004) or even a single photometric band (e.g., Neuhäuser et al. 2005; Metchev & Hillenbrand 2006). It is therefore appropriate to investigate how well the atmospheric parameters of L and T dwarfs can be determined by fitting L and T dwarf spectra over narrower wavelength ranges. In addition, we can also estimate the systematic errors in both the models and spectral fitting procedure by comparing how well the models fit the spectral features over narrower wavelength ranges as compared to the global 0.95–14.5 μm fits.

We therefore fit the data over the wavelength ranges described in § 4.3, as well as over the 0.95–2.5 μm wavelength range. For the IRS/SL and *Y*-, *J*-, *K*-, and *L*-band fits, we set $w_i = 1$ for all i. Table 5 lists the results of the fits, and Figure 13, which is similar to the bottom panel of Figure 5, shows the corresponding $T_{\rm eff}$ values for each dwarf. Figures 14–19 show the spectra and best-fitting models (*green lines*) along with the best-fitting models obtained by fitting the 0.95–14.5 μm spectrum (*red lines*, same as Fig. 6).

As expected, the model spectra fit the data much better over these narrower wavelength ranges. In most cases, remarkably good fits are obtained. However, the $T_{\rm eff}$ values derived from narrower wavelength ranges do not agree with those derived by fitting the 0.95–14.5 μm SEDs. Particularly poor $T_{\rm eff}$ values are derived by fitting the *L* band and IRS/SL spectra of the early- to mid-type L dwarfs (see Fig. 13). Below, we describe how the model spectra fit the data over the narrower wavelength ranges in more detail. Since the majority of the *H* band is not included in the fitting process (see § 4.1), we do not present a detailed description of that wavelength region below.

4.4.1. *Y-Band Fits*

Figure 14 shows the spectra and best-fitting model spectra over the *Y* band. The fits reproduce the overall shape of the *Y*-band data considerably better than the 0.95–14.5 μm fits for all spectral types. The remaining discrepancies highlight problems with specific molecular bands. The model FeH band heads at 0.9896 μm are still too weak, the 0.9969 μm CrH band heads are still present, and the TiO band heads at ∼1.104 μm are still too strong. Indeed, the CrH band head is present in all the model spectra shown in Figure 14. The strength of the ∼1.06 μm VO band is, however, much better matched when fitting the *Y*-band data alone. The peak flux of 2MASS 0559−1404 (T4.5) is also better matched when fitting the *Y*-band data alone, but the synthetic spectrum does exhibit the VO band that is absent from the data.

As shown in Figure 13, six of the nine dwarfs have derived $T_{\rm eff}$ values that fall within the Golimowski et al. (2004) effective temperature range. However, the derived $T_{\rm eff}$ values for the early- to mid-type L dwarfs (L1–L5) differ by no more than 200 K, while the Golimowski et al. (2004) 3 Gyr effective temperatures and the $T_{\rm eff}$ values derived by fitting the 0.95–14.5 μm spectra vary by 500 K over the same spectral-type range, which indicates that the *Y* band is not a sensitive indicator of effective temperature at these spectral types.

4.4.2. *J-Band Fits*

Figure 15 shows the spectra and best-fitting models over the 1.1–1.34 μm wavelength range. Fits to the *J*-band spectra alone significantly improve for those dwarfs where the global fit is rather

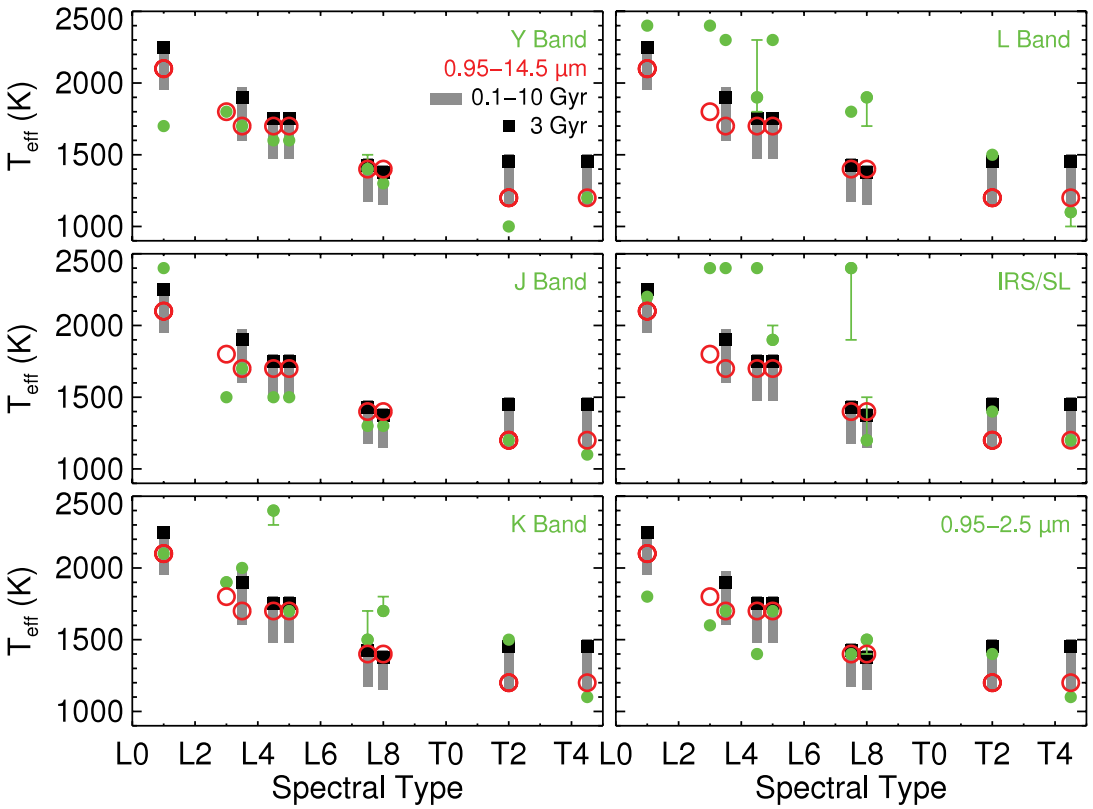

FIG. 13.—Summary of the best-fitting $T_{\rm eff}$ values (*green circles*) over the *Y*, *J*, *K*, and *L* bands, as well as the IRS/SL and the 0.95–2.5 μm wavelength ranges. Shown as open red circles are the best-fitting $T_{\rm eff}$ values derived by fitting the 0.95–14.5 μm spectra. Error bars denote the range of $T_{\rm eff}$ values for the models with $f_{\rm MC} > 0.1$. The gray regions denote the $T_{\rm eff}$ range corresponding to an age range of 0.1–10 Gyr, and the black squares denote the $T_{\rm eff}$ corresponding to 3 Gyr (Golimowski et al. 2004).

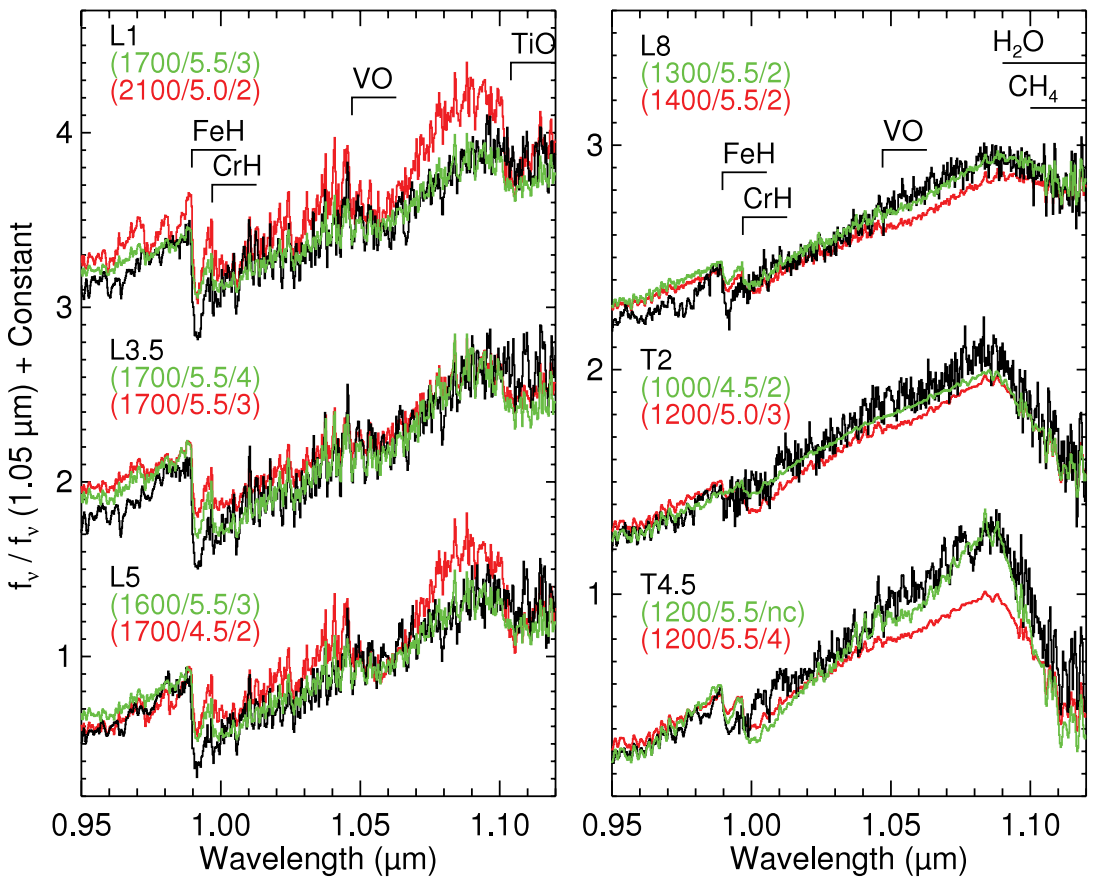

FIG. 14.—*Y*-band spectra of 2MASS 1439+1929 (L1), 2MASS 0036+1821 (L3.5), 2MASS 1507−1627 (L5), DENIS 0255−4700 (L8), SDSS 1254−0122 (T2), and 2MASS 0559−1404 (T4.5) (*black lines*). The data have been normalized to unity at 1.05 μm and offset for clarity. The best-fitting models ($T_{\rm eff}$/log g/$f_{\rm sed}$) are shown in green, as well as the best-fitting models (*red*) obtained from fitting the entire 0.95–14.5 μm spectrum. The models have been normalized and offset with the same constants as the data and multiplied by the constant *C* (see § 4.1) before normalization to preserve the relative flux levels between the data and models.

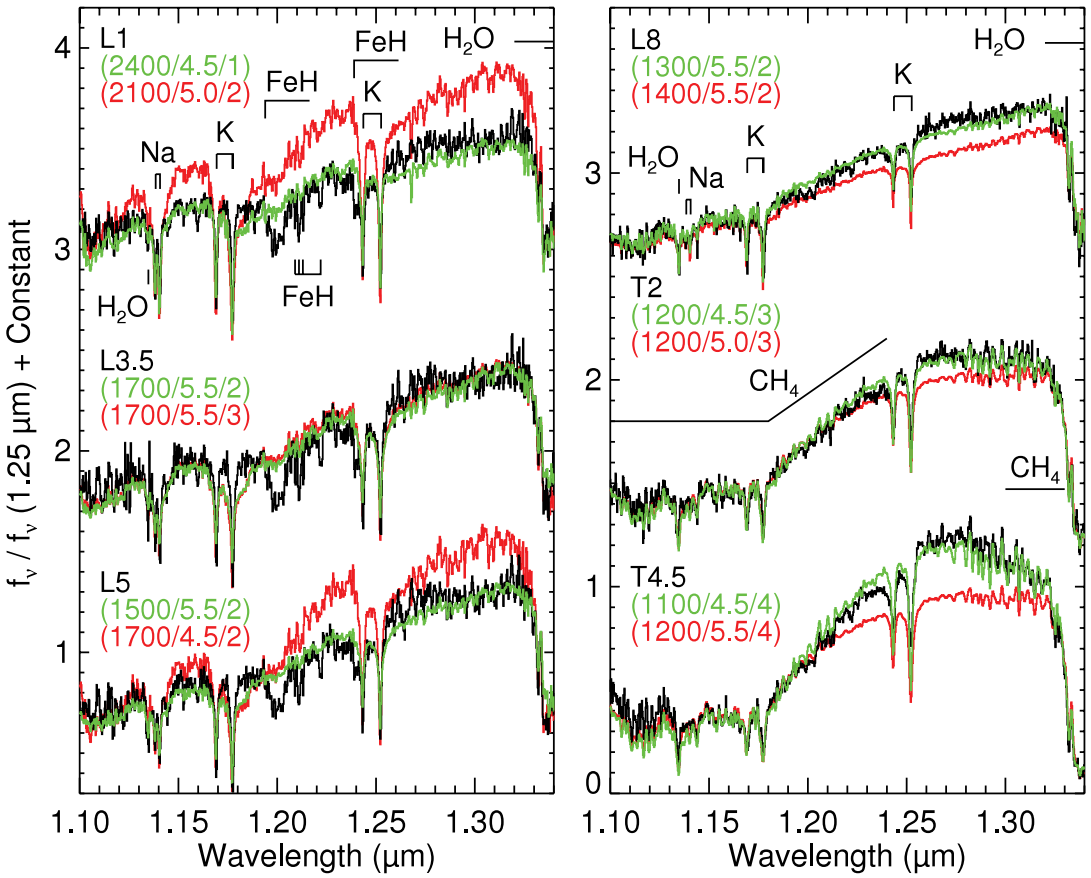

FIG. 15.—Same as Fig. 14, except the data cover the *J* band and were normalized at 1.25 μm.

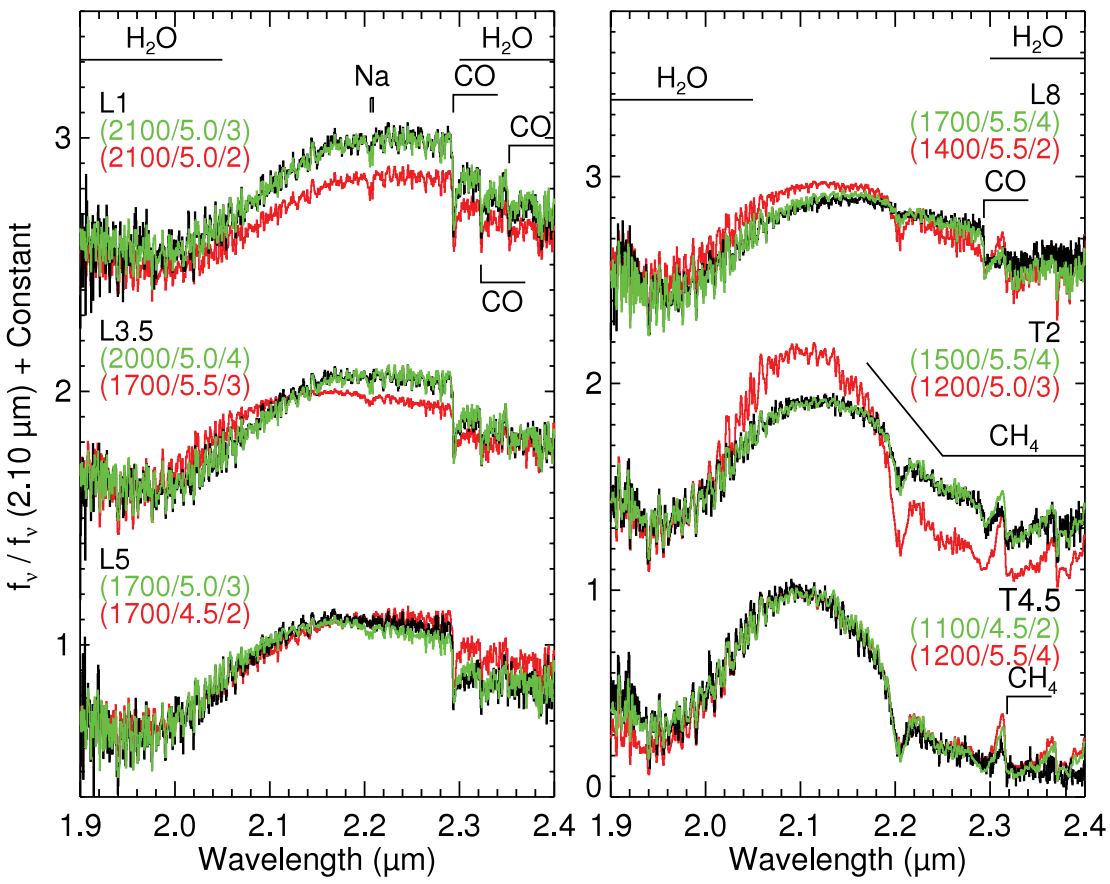

FIG. 16.—Same as Fig. 14, except the data cover the *K* band and were normalized at 2.1 μm.

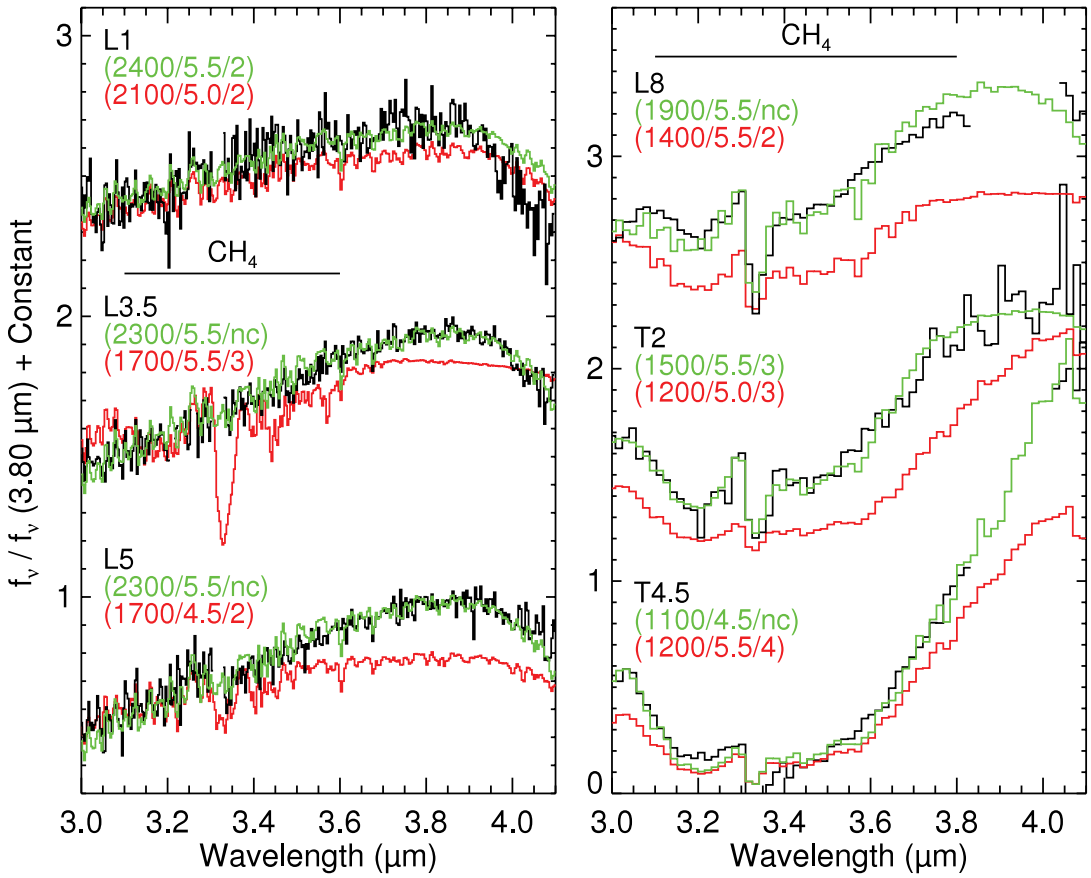

FIG. 17.—Same as Fig. 14, except the data cover the *L* band and were normalized at 3.8 μm.

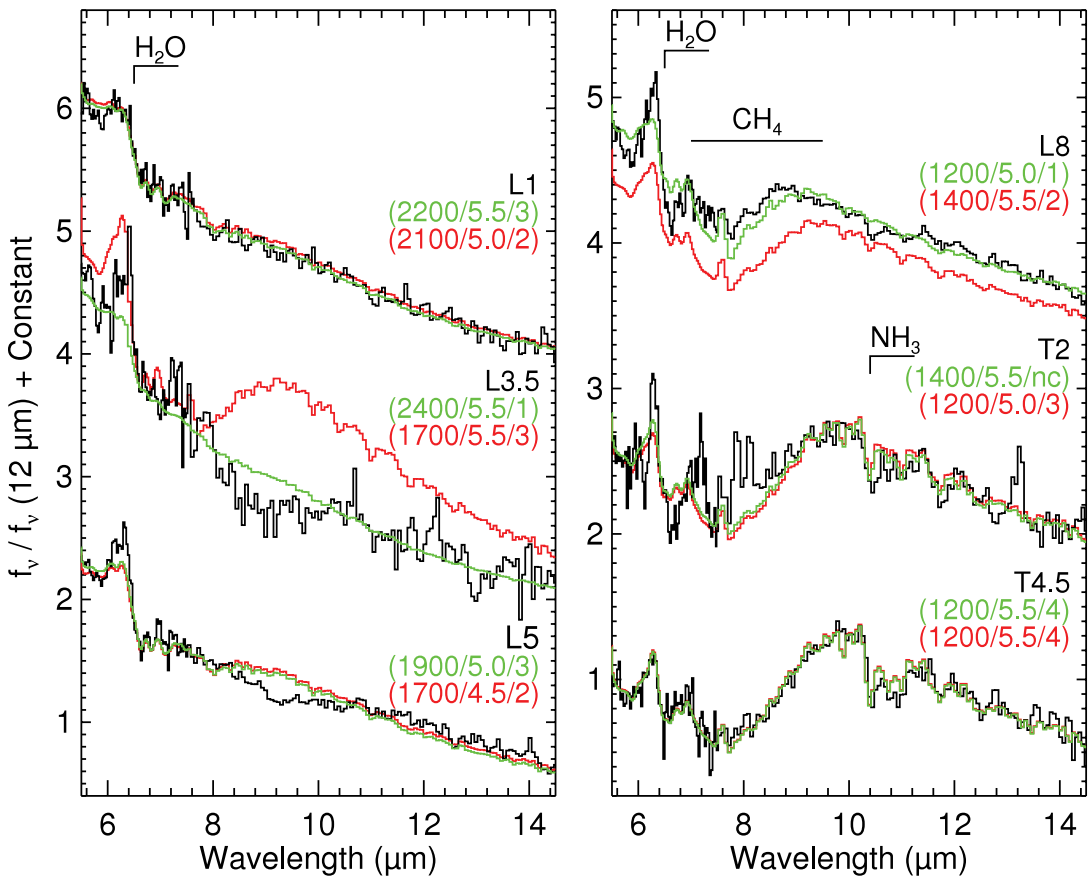

FIG. 18.—Same as Fig. 14, except the data cover the IRS/SL wavelength range and were normalized at 12 μm.